

1 **Global Monthly Ocean Dissolved Oxygen (1960 – 2023)**
2 **Reconstructed to 5,902 m with BLENDR, a Bayesian-**
3 **Optimized Ensemble Learning Framework**

4
5 Mingyu Han¹, Xiaogang Xing², Yuntao Zhou^{1*}

6 1. School of Oceanography, Shanghai Jiao Tong University, Shanghai, China

7 2. State Key Laboratory of Satellite Ocean Environment Dynamics (SOED), Second
8 Institute of Oceanography, Ministry of Natural Resources, Hangzhou, China

9 Corresponding author

10 *Correspondence to: Yuntao Zhou, ytzhou@sjtu.edu.cn, ORCID: 0000-0001-9714-5385

11

12 **Abstract**

13 Oceanic oxygen levels, crucial for marine ecosystems and biogeochemical cycles, have declined
14 significantly over the past few decades due to climate change, posing severe environmental risks.
15 However, historical dissolved oxygen (DO) measurements, especially below 2,000 m, remain sparse,
16 limiting comprehensive annual and seasonal analyses. Here, we introduce the BLENDR framework
17 (Bayesian-optimized Learning and ENsemble modeling for Data Reconstruction), a Bayesian-
18 optimized ensemble of six machine-learning models (Random Forest, XGBoost, LightGBM,
19 CatBoost, Extremely Randomized Trees and Histogram-based Gradient Boosting) fused via [a](#)
20 [spatially coherent dynamic weighting scheme](#)~~dynamic weighting~~, to reconstruct global monthly
21 DO distributions at a $1^\circ \times 1^\circ$ resolution from the surface to 5,902 m from 1960 to 2023.
22 Validation against an independent dataset demonstrated that BLENDR achieves [better](#)
23 [performance](#)~~lower errors~~ than any individual model, [with an \$R^2\$ of 0.968](#). Our dataset captures
24 depth-dependent deoxygenation, with the most pronounced decline occurring between 150 and
25 200 m [at approximately \$-0.12 \mu\text{mol kg}^{-1} \text{yr}^{-1}\$](#) , and [shows](#)~~reveals~~ severely accelerated oxygen loss
26 in the Arctic Ocean and North Atlantic over the past decade. This work provides [the first](#) long-
27 term, global monthly DO product from the ocean surface to 5,902 m. The bathypelagic DO data
28 provided in this work is a significant contribution to deep ocean oxygen dynamics and global
29 biogeochemical cycles. [The data product is publicly accessible at](#)
30 <https://doi.org/10.5281/zenodo.19705526> (Han and Zhou, 2026).

31 **Keywords**

32 dissolved oxygen, machine learning, ensemble learning, Bayesian optimization, data
33 reconstruction

34 **1 Introduction**

35 Over the past few decades, dissolved oxygen (DO) levels in open oceans have been rapidly
36 decreasing (Breitburg et al., 2018; Keeling et al., 2010), primarily driven by climate change (Deutsch
37 et al., 2011). This continuous decline has severely affected marine organisms and ~~biogeochemical~~
38 ~~processes~~ ocean chemistry, disrupting marine productivity, and biodiversity, ~~and biogeochemical~~
39 ~~cycles~~ (Gruber, 2011; Stramma et al., 2012). Climate models predict that global warming will
40 further accelerate this deoxygenation (Oschlies et al., 2018), potentially adversely affecting aerobic
41 marine organisms within this century (Sampaio et al., 2021) and altering biogeochemical cycles
42 (Gruber, 2004; Berman-Frank et al., 2008). Therefore, it is important to develop a comprehensive,
43 high-resolution reconstruction of ocean DO across both space and depth to accurately quantify
44 historical deoxygenation trends, identify regional hotspots, and inform future ecosystem and
45 climate projections.

46
47 Despite significant progress in oceanographic data collection, severe gaps in historical DO data
48 persist, hindering comprehensive analysis. For instance, the World Ocean Database (WOD)
49 (Mishonov et al., 2024) compiles DO profiles from research cruises and floats, yet observations
50 remain sparse and unevenly distributed across much of the global ocean ~~most ocean regions still~~
51 ~~lack any observations~~. This sparse spatial coverage severely limits the use of data imputation
52 methods to reconstruct four-dimensional DO fields. Furthermore, although many Earth System
53 Models (ESMs) attempt to simulate global oceanic DO, these models are not directly constrained
54 by historical DO observations in the way observation-based reconstructions are, ~~lack adjustments~~
55 ~~based on DO observation data~~, leading to error propagation (Pathak et al., 2023). Thus, numerical
56 models diverge significantly from *in situ* observations and ~~consistently~~ underestimate actual DO
57 decline trends (Bopp et al., 2013; Cocco et al., 2013; Long et al., 2016; Kwiatkowski et al., 2020),
58 which reduces confidence in model-based assessments of ocean deoxygenation, Oxygen Minimum
59 Zones (OMZ), and biogeochemical cycles.

60
61 Classical interpolation methods have long been employed to map oceanic DO. Zhou et al. (2022)
62 combined geostatistical regression with Monte Carlo methods to estimate changes in the area of
63 OMZs globally and regionally from 1960 to 2019. Garcia et al. (2024) applied objective analysis in
64 the World Ocean Atlas 2023 (WOA23) to produce internally consistent annual and monthly DO
65 fields from 1965 to 2022. Gouretski et al. (2024) developed an automated quality control
66 procedure to detect outliers and correct biases in ocean oxygen profiles, producing a consistent
67 global dataset from 1920 to 2023. Roach and Bindoff (2023) used Data Interpolating Variational
68 Analysis (DIVA) to generate a global high-resolution oxygen atlas from 1955 to 2018.

69
70 Recently, machine learning approaches have been increasingly adopted in Earth system science
71 and oceanography because they can efficiently exploit large datasets and capture complex

72 nonlinear relationships (Reichstein et al., 2019; Shen, 2018). Giglio et al. (2018) utilized a random
73 forest regression model to estimate the oxygen concentration at 150 m in the Southern Ocean on
74 the basis of Argo data from 2008 to 2012. Sharp et al. (2023) reconstructed a global DO dataset
75 called GOBAI-O₂ using feedforward neural networks and random forest regression, spanning the
76 years 2004–2022 with a monthly resolution and extending from the ocean surface to a depth of
77 2,000 m. Ito et al. (2024) developed a machine-learning ensemble of neural networks and random
78 forests trained on historical shipboard and biogeochemical Argo DO profiles to generate gridded
79 monthly oxygen fields. Crucially, most existing machine-learning reconstructions are limited to the
80 upper 2,000 m of the water column, leaving the vast bathypelagic zone (below 2,000 m) poorly
81 constrained, despite its importance for global carbon storage and long-term oxygen budgets. While
82 some of the DO data reconstruction studies focus on specific regions (Giglio et al., 2018; Huang et
83 al., 2023), some span longer time spans (Roach and Bindoff, 2023; Ito et al., 2024), and some
84 achieve higher temporal or spatial resolutions (Sharp et al., 2023; Shao et al., 2023), it is challenging
85 to simultaneously address all aspects.

86
87 Here, we introduce the BLENDR framework (Bayesian-optimized Learning and ENsemble modeling
88 for Data Reconstruction), which integrates six tree-based learners, Random Forest, XGBoost,
89 LightGBM, CatBoost, Extremely Randomized Trees and Histogram-based Gradient Boosting, each
90 tuned via Bayesian hyperparameter optimization. Model outputs are fused with [a spatially
91 coherent dynamic weighting scheme that combines global prior model skill with locally constrained
92 error information.](#)~~dynamic weights combining global cross-validation skill and local error
93 performance.~~ BLENDR produces a global 1° × 1° monthly DO dataset from 1960 to 2023 down
94 to 5,902 m, filling critical deep-ocean gaps. We evaluated the ensemble using 8-fold temporal
95 cross-validation and an independent [filtered](#) subset of the Global Ocean Data Analysis Project
96 v2.2023 (GLODAPv2) (Olsen et al., 2016) after all the profiles that overlap with the WOD (CTD and
97 OSD) collections were removed to ensure independence. We also quantified the measurement,
98 grid and algorithm uncertainties. Using this product, we analyzed global, basin-scale and depth-
99 resolved DO distributions and long-term deoxygenation trends, including the vertical structure and
100 multi-basin evolution of OMZ extent, changes in basin-scale oxygen content and their recent
101 acceleration, and hemispheric differences in DO seasonality. In addition, we quantified the
102 influence of a recently documented systematic bias in delayed-mode Argo DO by comparing
103 reconstructions with and without a [system-uniform](#) correction applied to Argo profiles. To capture
104 regional differences in oxygen storage and trends, we divided the global ocean into ten basins: the
105 North Pacific (NP), Equatorial Pacific (EP), South Pacific (SP), North Atlantic (NA), Equatorial Atlantic
106 (EA), South Atlantic (SA), North Indian (NI), South Indian (SI), Southern Ocean (SO) and Arctic Ocean
107 (AO). The basin boundaries (Figure [6a1](#)) follow Schmidtko et al. (2017).

109 2 Data and methods

110 2.1 Data

111 2.1.1 Observational data of dissolved oxygen

112 We assembled our observational DO database by merging quality-controlled profiles from the
113 Array for Real-Time Geostrophic Oceanography dataset (Argo, <https://argo.ucsd.edu>) (Wong et

114 al., 2020) with Conductivity-Temperature-Depth (CTD) and Ocean Station Data (OSD)
115 measurements archived in the World Ocean Database 2023 (WOD,
116 <https://www.ncei.noaa.gov/products/world-ocean-database>) (Mishonov et al., 2024). Each
117 profile consists of oxygen concentrations ~~sampled-measured~~ at multiple depths at a given date
118 and location. For Argo, we restricted the data to post-processed delayed-mode profiles and
119 retained only records flagged as good. Overlapping profiles were deduplicated by keeping the
120 version with finer vertical sampling. Although we initially followed Schmidtko et al. (2017) in
121 treating the combined dataset as free of systematic errors, recent evidence indicates a systematic
122 offset between Argo and CTD/OSD. Accordingly, following Wang et al. (2025), we applied a
123 uniform $+1.69 \mu\text{mol kg}^{-1}$ bias correction to all delayed-mode Argo DO profiles. Annual profile
124 counts of OSD, CTD, and Argo observations are shown in Figure S1. Although DO observations
125 below 2,000 m become sparser with depth, they remain available across most basins (Table S1).

126 To obtain an independent evaluation set, we constructed a validation subset from GLODAPv2
127 (Olsen et al., 2016) after removing any profiles that overlap with our training pool from CTD and
128 OSD. We compared the two collections profile by profile and applied a conservative space and
129 time filter: for each oxygen profile in GLODAPv2, we searched the CTD and OSD records for
130 profiles within $\pm 1^\circ$ in longitude, $\pm 1^\circ$ in latitude, and the same calendar month. When
131 such a match existed, we treated the pair as duplicates and excluded the GLODAPv2 profile from
132 validation. This reduced the original 56,480 GLODAPv2 profiles to 8,020. The spatial distribution
133 and temporal histograms of the filtered GLODAPv2 dataset are shown in Figure S2. A manual spot
134 check confirmed that no additional space-time matches remained. We therefore use this filtered
135 ~~GLODA-GLODAPv2~~ dataset as a robust and an independent benchmark for assessing our
136 reconstruction.

137 **2.1.2 Reanalysis data of environmental factors**

138 We obtained monthly ocean temperature (T, °C), salinity (S, PSU), meridional velocity and zonal
139 velocity (MV and ZV, m s^{-1}) from the Ocean Reanalysis System 5 (ORAS5) gridded ocean dataset
140 with a spatial resolution of $0.25^\circ \times 0.25^\circ$ and 75 vertical levels (Table ~~S1~~S2), ranging from the
141 ocean surface to 5,902 m in depth (<https://cds.climate.copernicus.eu/datasets/reanalysis-oras5>).
142

143 **2.2 BLENDR framework**

144 We developed the BLENDR framework to reconstruct a global, monthly DO product from 1960
145 through 2023. The process began by assembling and preprocessing all available *in situ* DO profiles
146 ~~alongside together with~~ key environmental factors (T, S, and currents) onto a monthly grid featuring
147 ~~a $1^\circ \times 1^\circ$ horizontal resolution and grid with~~ 75 vertical levels. Next, each of the six tree-based
148 learners (Random Forest, XGBoost, LightGBM, CatBoost, Extremely Randomized Trees and
149 Histogram-based Gradient Boosting) underwent Bayesian hyperparameter tuning via Optuna's
150 Tree-structured Parzen Estimator (TPE) sampler, ensuring that each model minimized the cross-
151 validation RMSE (Akiba et al., 2019). Once optimized, the models were trained on the full gridded
152 dataset and predicted the DO concentration at every valid grid cell, producing six complete four-
153 dimensional DO fields. These outputs were then merged through a spatially coherent dynamic
154 weighting scheme (Dietterich, 2000). This approach assigns prior weights based on each model's
155 temporal cross-validation skill, derives locally varying weights from model agreement with
156 available observations, and then propagates these local weights to neighboring grid cells through

Gaussian kernel smoothing while gradually shrinking them toward the prior weights as observational support decreases. The resulting ensemble therefore adapts continuously in space while retaining stable behavior in poorly observed regions. Finally, model performance was assessed using 8-fold temporal cross-validation and an independent evaluation against the filtered GLODAPv2 dataset (Olsen et al., 2016). The overall workflow of the BLENDR framework is shown in Figure 1. This approach uses prior weights based on each model's time cross-validation skill and adjusts them locally with "dynamic" weights that reflect agreement with nearby observations, yielding an ensemble that adapts in space and time. Finally, we validated and quantified the performance by conducting 8-fold temporal cross-validation, an independent evaluation against GLODAPv2 (Olsen et al., 2016).

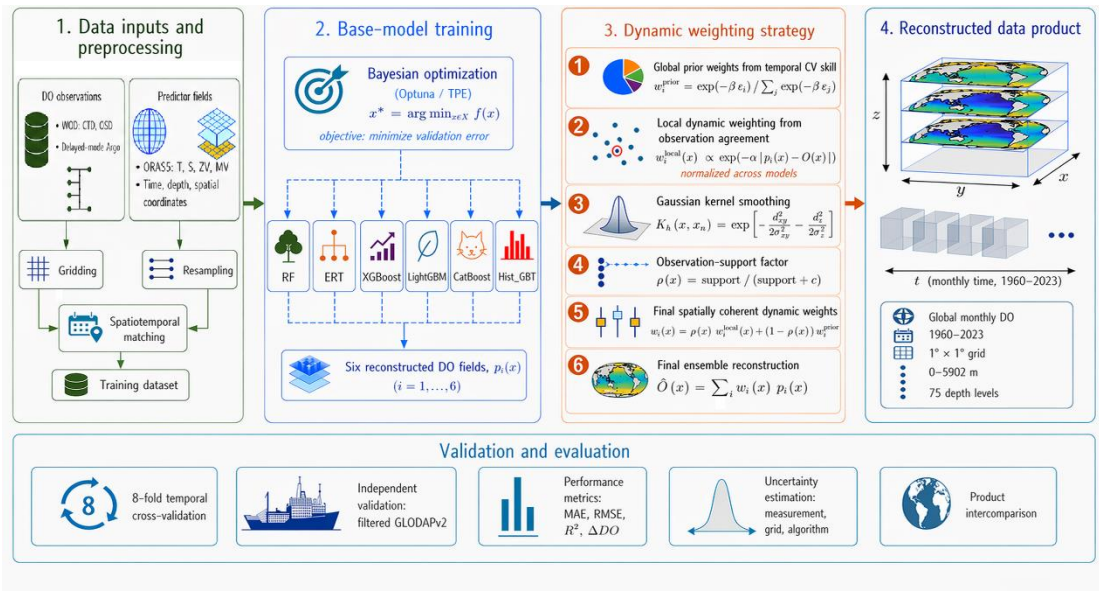


Figure 1. Overview of the BLENDR framework.

2.2.1 Data processing

In this study, all ocean DO observation data included temporal and spatial information, such as the year, month, day, longitude, latitude, and measurement depth. The longitude and month are both periodic features. For instance, longitude ranges from 0° to 360° , with 360° overlapping with 0° , and month indexes represents an annual cycle that repeats every 12 months. To address this issue, we followed the approach of Gade (2010) and Tang et al. (2019) by converting the representing longitude and month attributes to polar coordinate systems using sine and cosine functions.

Although ORAS5 is provided on a $0.25^\circ \times 0.25^\circ$ grid, we upscaled it by simple averaging to a common $1^\circ \times 1^\circ$ grid with 75 depth levels. For each 1° grid cell, we averaged all available ORAS5 values located within that cell. DO observations were binned to each grid cell by averaging all points that fell within the cell at the same month and depth level. To address potential multicollinearity, which can lead to instability in subsequent modeling and increase the risk of overfitting, we analyzed correlations between the 11 factors. No correlation coefficient exceeded 0.5, so variable selection was not necessary in this case (Figure S2S3). A complete list of predictors, with abbreviations and data sources, is shown in Table 1.

Table 1. Predictors, abbreviations and products/references of the 11 environmental factors.

Predictor	Abbreviation	Product/Reference
$\sin(\text{latitude} \cdot \pi/180)$	coord_1	WOD (CTD+OSD) & Argo
$\sin(\text{longitude} \cdot \pi/180) \cdot \cos(\text{latitude} \cdot \pi/180)$	coord_2	
$-\cos(\text{longitude} \cdot \pi/180) \cdot \cos(\text{latitude} \cdot \pi/180)$	coord_3	
Year	Year	
$\cos(\text{month} \cdot 2\pi/12)$	time_cos	
$\sin(\text{month} \cdot 2\pi/12)$	time_sin	
Depth	Depth	
Temperature	T	ORAS5
Salinity	S	
Zonal Velocity	ZV	
Meridional Velocity	MV	

187 Note: The observational data were from WOD and Argo. The data from ORAS5 were $0.25^\circ \times 0.25^\circ$
188 monthly mean profile data.

189

190 2.2.2 Machine learning models

191 We used six tree-based algorithms to reconstruct dissolved oxygen. Each model offers a different
192 balance of bias, variance, and speed/computational efficiency. We chose them because of their
193 robust performance in regression tasks and their ability to handle nonlinear relationships. We
194 used six models because they span the main tree learning paradigms, namely, bagging and
195 boosting; thus, their strengths are complementary, and their residual errors are expected to be
196 only weakly correlated. We kept the ensemble within the tree family because dissolved oxygen
197 depends on nonlinear interactions among multiple drivers, and the data contain missing values,
198 ~~which are~~ conditions in-under which decision trees perform well without elaborate feature
199 engineering. In our initial model screening under the same input features and validation
200 framework, the tested neural-network models, including a convolutional neural network and a
201 back-propagation neural network, did not show an accuracy advantage over Random Forest,
202 while requiring more tuning effort and providing less interpretability. Therefore, we focused the
203 final ensemble on tree-based learners.~~In preliminary trials with neural networks, we did not~~
204 ~~observe a consistent increase in skill, whereas interpretability and tuning became more difficult;~~
205 ~~thus, the tree ensemble offered the best balance for this application.~~ All the models were trained
206 on the same input features and tuned via Bayesian optimization (Sect. 2.2.3). Below, we briefly
207 describe each model.

208 Random Forest (RF) builds many decision trees on bootstrap samples and averages their outputs
209 (Breiman, 2001). It selects a random subset of features at each split. This randomness reduces
210 overfitting. RF handles large datasets well and is robust to outliers. RF represents classical
211 bagging, and Extremely Randomized Trees (ERTs) push this idea toward stronger randomness
212 (Geurts et al., 2006). It selects split thresholds at random rather than searching for the best cut. It
213 uses the full dataset rather than bootstrapping. This strong randomization further lowers
214 variance at modest cost in terms of bias. CatBoost is a gradient-boosting library designed for
215 categorical features (Prokhorenkova et al., 2018). It uses ordered target statistics to avoid target
216 leakage. It grows symmetric trees and performs efficient leaf pruning. CatBoost often converges

217 faster and requires less tuning of the learning rate. XGBoost implements gradient boosting with
 218 second-order optimization (Chen & Guestrin, 2016). It adds regularization to control the
 219 complexity of the tree. It uses approximate split finding to speed up training on large data.
 220 XGBoost balances accuracy and runtime efficiency. LightGBM uses histogram-based binning and
 221 leaf-wise tree growth (Ke et al., 2017). It buckets continuous features into bins, reducing the
 222 amount of memory. Trees grow by selecting splits that yield the greatest loss reduction.
 223 LightGBM is highly efficient for large feature sets and large datasets. Histogram-based Gradient
 224 Boosting (Hist_GBT) follows Friedman's original gradient boosting framework (Guryanov, 2019;
 225 Friedman, 2001). It fits a sequence of weak learners to the negative gradient of the loss. It also
 226 uses histogram binning for faster split evaluation. Hist_GBT offers good accuracy in high-
 227 dimensional settings. XGBoost, LightGBM and Hist_GBT are gradient boosting methods but differ
 228 in terms of split criteria and optimization details.

229 **2.2.3 Bayesian parameter optimization**

230 To optimize hyperparameters across different machine learning models in a systematic and
 231 efficient manner, we employed Bayesian optimization using the Optuna framework (Akiba et al.,
 232 2019). Unlike grid or random search, this approach builds a statistical model of how settings
 233 affect error and then tests promising regions more often, finding good configurations with fewer
 234 trials and providing a fair, comparable procedure across models. Specifically, at each trial, a
 235 candidate set of hyperparameters is sampled, the model is trained, and its validation error is
 236 recorded. Optuna then uses all the previously tested hyperparameter–error pairs to update the
 237 surrogate model and proposes the next set of hyperparameters where the error is expected to
 238 decrease.

239 Bayesian optimization was used to construct a probabilistic surrogate model of the objective
 240 function $f(x)$, where x is a vector of hyperparameters. The optimization seeks to identify the
 241 optimal x^* that minimizes f :

$$242 \quad x^* = \arg \min_{x \in \chi} f(x) \quad (1)$$

243 Here, χ denotes the hyperparameter space. In practice, we used the Tree-structured Parzen
 244 Estimator (TPE) sampler in Optuna to approximate the objective function. After each trial, the
 245 observed pairs $(x, f(x))$ are divided into a “good” set with low objective values and a “bad” set
 246 with high values, using a quantile threshold. The TPE then fits two probability density functions
 247 over the hyperparameters, one for the good set and one for the bad set, and proposes new
 248 candidates in regions where the ratio of these densities is large. This strategy is equivalent to
 249 selecting the next sampling point to maximize the Expected Improvement (EI):

$$250 \quad EI(X) = \int_{-\infty}^{y^*} (y^* - y) \cdot p(y | x) dy \quad (2)$$

251 where y^* is the current best objective value. The sampling focuses on regions with high EI. In
 252 plain terms, the EI favors trials that are expected to reduce the error relative to the current best,
 253 so the search is concentrated on the most promising parts of the space.

254 To reduce temporal overfitting and preserve model generalizability across decades,
 255 hyperparameter optimization was conducted using a subset of data from eight years (1960, 1968,
 256 1976, 1984, 1992, 2000, 2008, 2016). These years were chosen to sample different climate and
 257 sampling regimes across the six-decade period, ensuring that the optimized models are robust to
 258 temporal shifts in data availability and underlying oceanic conditions. The objective function
 259 minimized the Mean Squared Error (MSE) on an independent validation set derived from eight
 260 other test years (1967, 1975, 1983, 1991, 1999, 2007, 2015, and 2023). We chose the MSE
 261 because it penalizes large errors more heavily, which is desirable when evaluating gridded oxygen
 262 where occasional large deviations can dominate downstream diagnostics. The objective function
 263 was defined as follows:

$$264 \quad MSE = \frac{1}{n} \sum_{i=1}^n (\hat{y}_i - y_i)^2 \quad (3)$$

265 Each model was optimized over its own hyperparameter space, with the best-performing
 266 configuration recorded for final training and subsequent prediction on independent test data.
 267 This consistent, data-driven approach ensured fair comparability across all six learners and
 268 minimized bias from manual tuning. Below, we summarize the search space and optimal
 269 parameters in Table 2.

270 **Table 2. Hyperparameter search spaces and optimal values**

Model	Hyperparameter	Search Range	Best Value
ERT	n_estimators	50 - 500	452
	max_depth	3 - 20	20
	min_samples_split	2 - 20	15
	min_samples_leaf	1 - 10	2
	max_features	0.1 - 1.0	0.577
	bootstrap	{True, False}	False
CatBoost	iterations	50 - 1000	950
	depth	3 - 12	12
	learning_rate	0.005 - 0.3	0.077
	l2_leaf_reg	10^{-5} - 10	0.009
	random_strength	10^{-5} - 10	7.053×10^{-5}
	bagging_temperature	0 - 1	0.122
	border_count	32 - 255	120
Hist_GBT	learning_rate	0.005 - 0.3	0.177
	max_iter	50 - 1000	928
	max_depth	3 - 12	8
	min_samples_leaf	5 - 50	41
	l2_regularization	10^{-5} - 10	0.932

	max_bins	32 - 255	251
LightGBM	n_estimators	50 - 1000	954
	max_depth	3 - 12	12
	learning_rate	0.005 - 0.3	0.264
	num_leaves	10 - 300	145
	min_child_samples	5 - 50	18
	subsample	0.5 - 1.0	0.683
	colsample_bytree	0.5 - 1.0	0.828
	reg_alpha	10^{-8} - 10	6.15×10^{-7}
	reg_lambda	10^{-8} - 10	4.708
RF	num_trees	10 - 200	87
	min_leaf_size	10 - 100	10
XGBoost	n_estimators	50 - 1000	138
	max_depth	3 - 12	12
	learning_rate	0.005 - 0.3	0.256
	min_child_weight	1 - 10	5
	subsample	0.5 - 1.0	0.922
	colsample_bytree	0.5 - 1.0	0.599

271

272 2.2.4 Multi-model fusion and dynamic weighting **strategyscheme**

273 We fused the predictions of the six base models into a single reconstruction using a spatially
274 coherent dynamic weighting scheme. The aim was to combine global model skill with local
275 observational constraint while maintaining spatial continuity in the weight field. This formulation
276 is consistent with ensemble weighting based on model skill, locally calibrated weighting informed
277 by nearby observations, and kernel-based estimation for spatially varying relationships (Raftery et
278 al., 2005; Kleiber et al., 2011; Brunson et al., 1996). Each model was first assigned a global prior
279 weight derived from its average predictive skill in temporal cross-validation. These prior weights
280 served as a stable baseline in regions with weak observational support. We then introduced locally
281 varying weights based on the agreement between model predictions and available observations.
282 To avoid abrupt spatial changes in the weights, the local weights were further propagated to
283 neighboring grid cells through Gaussian kernel smoothing and were gradually shrunk toward the
284 global prior weights as observational support decreased.

285 We define the global prior weight ω_i of model i from its MAE ϵ_i in temporal cross-validation (Sect.
286 3.1) as

$$287 \omega_i = \frac{\exp(-\beta\epsilon_i)}{\sum_{j=1}^M \exp(-\beta\epsilon_j)} \quad (4)$$

288 where $M=6$ is the number of base models and β is the prior-weight sensitivity parameter. A smaller
289 ϵ_i gives a larger ω_i , so models with better overall performance receive higher prior weights. Here,
290 β controls how strongly the prior weights respond to differences in model MAE. We set $\beta=1$ to
291 preserve the relative performance differences among models while avoiding excessively
292 concentrated prior weights.

293 At grid cells with valid observations, we first define the local score of model i as

$$294 \quad s_i(x) = \exp(-\alpha | p_i(x) - O(x) |) \quad (5)$$

295 where $p_i(x)$ is the prediction of model i at grid cell x, $O(x)$ is the observed value. Here, α controls
296 the sensitivity of local weighting to model error. We set $\alpha=1$ to preserve the influence of local
297 model-observation mismatch while avoiding excessively sensitive weight adjustments. These local
298 scores are then normalized across all models to obtain the effective local weight at observation-
299 supported grid cells:

$$300 \quad l_i^{obs}(x) = \frac{s_i(x)}{\sum_{j=1}^M s_j(x)} \quad (6)$$

301 To extend the observational constraint smoothly to neighboring locations, we applied Gaussian
302 kernel smoothing to the effective local weights. The kernel is defined as

$$303 \quad K_h(x, x_n) = \exp\left(-\frac{d_{xy}(x, x_n)^2}{2\sigma_{xy}^2} - \frac{d_z(x, x_n)^2}{2\sigma_z^2}\right) \quad (7)$$

304 where x_n denotes a neighboring grid cell, $d_{xy}(x, x_n)$ is the horizontal distance between x and x_n ,
305 $d_z(x, x_n)$ is the vertical distance, and σ_{xy} and σ_z control the smoothing scales in the horizontal and
306 vertical directions, respectively. The smoothed local weight of model i is then written as

$$307 \quad \tilde{l}_i(x) = \frac{\sum_{x_n \in N(x)} K_h(x, x_n) l_i^{obs}(x_n)}{\sum_{x_n \in N(x)} K_h(x, x_n)} \quad (8)$$

308 where $N(x)$ is the set of neighboring grid cells with valid effective local weights.

309 To quantify the degree of local observational support around each grid cell, we define

$$310 \quad S(x) = \sum_{x_n \in N(x)} K_h(x, x_n) \quad (9)$$

311 and then construct an observation-support factor as

$$312 \quad \rho(x) = \frac{S(x)}{S(x) + c} \quad (10)$$

313 where c is a shrinkage parameter. When observational support is strong, $\rho(x)$ approaches 1 and
314 the final weight is mainly controlled by the smoothed local weight. When observational support is
315 weak, $\rho(x)$ decreases and the final weight gradually returns toward the global prior weight.

316 Accordingly, the final weight of model i at grid cell x is defined as

$$317 \quad w_i(x) = \rho(x) \tilde{l}_i(x) + [1 - \rho(x)] \omega_i \quad (11)$$

318 The final ensemble reconstruction is then calculated as

319
$$\hat{O}(x) = \sum_{i=1}^M w_i(x) p_i(x) \tag{12}$$

320 We fused the six model predictions into one field. Our goal was to combine global model skill with
 321 local fit to observations. We assigned each model a static “prior” weight. The prior serves as a
 322 baseline that reflects each model’s average skill over time and space and provides a stable fallback
 323 where observations are sparse or absent; thus, the fusion does not chase noise in poorly sampled
 324 regions. We then adjusted those weights at each grid cell using the local agreement between the
 325 prediction and observation. This second step allows for nearby observations to steer the fusion so
 326 that, where data exist, models that match them contribute more.

327 We derive a prior weight ω_i for Model i from its time-cross-validation (Sect. 3.1) RMSE ϵ_i . We set
 328 a decay parameter β . Then,

329
$$\omega_i = \frac{\exp(-\beta \epsilon_i)}{\sum_{j=1}^6 \exp(-\beta \epsilon_j)}, \sum_{i=1}^6 \omega_i = 1 \tag{4}$$

330 A smaller ϵ_i yields a larger ω_i . We chose $\beta=1$ to balance the influence among the models. β controls
 331 how quickly low-error models dominate, and $\beta=1$ rewards better performers without collapsing
 332 diversity.

333 At each grid cell x , we compute a dynamic weight $v_i(x)$. We use a tuning parameter α . For cells
 334 where an observation $O(x)$ exists, we set the following equation:

335
$$v_i(x) = \exp(-\alpha |p_i(x) - O(x)|) \tag{5}$$

336 Here, $p_i(x)$ is model i ’s prediction. A smaller local error makes $v_i(x)$ larger. We used $\alpha=1$. The
 337 parameter α indicates how strongly local mismatch reshapes the weights, and $\alpha=1$ provided the
 338 best trade-off between responsiveness to local observations and stability in cross-validation tests.
 339 For cells with no observation, we used the static weight as follows:

340
$$v_i(x) = \omega_i \tag{6}$$

341 We computed the ensemble prediction $E(x)$ by normalizing the dynamic weights:

342
$$E(x) = \frac{\sum_{i=1}^6 v_i(x) p_i(x)}{\sum_{i=1}^6 v_i(x)}, \text{ if } \sum_i v_i(x) > 0 \tag{7}$$

343 and $E(x)=\text{NaN}$ if all $p_i(x)$ are missing. This formula guarantees that models aligning well with local
 344 observations gain more influence, while the static weights keep poorly observed regions stable.

345 2.2.5 Data reconstruction

346 We produced a global, monthly DO dataset on a regular $1^\circ \times 1^\circ$ grid and 75 depth levels (0–
 347 5,902 m) spanning from 1960 to 2023. First, we gathered all the predictor fields described in
 348 Table 1. Each field was remapped to the target grid and monthly time step following consistent
 349 with ORAS5. Next, we applied the six optimized machine-learning models (Sect. 2.2.2) at every

valid grid cell and time [step](#). Each model ingested the full vector of predictors and returned a DO estimate only where all ~~the~~ predictors were [present/available](#). This yielded six parallel prediction arrays with dimensions 360 (longitude) × 180 (latitude) × 75 (depth ~~levels~~) × 12 (months) × 64 (years from 1960 to 2023). We then merged these arrays using our [spatially coherent](#) dynamic weighting scheme (Sect. 2.2.4). [Global prior weights reflected each model’s cross-validation skill, whereas locally varying weights were derived from model agreement with available in situ observations. These local weights were then propagated to neighboring grid cells through Gaussian kernel smoothing and gradually shrunk toward the prior weights as observational support decreased.](#) ~~Static “prior” weights reflect each model’s cross-validation skill. Local weights adapt to agree with any overlapping in situ observations.~~ The weighted combination produces a single ensemble DO field ~~at~~ [for](#) each grid cell and month. We packaged the ensemble field into a NetCDF file with coordinate variables, depth layers, time axes, and global attributes documenting the [dataset](#) and methods.

2.2.6 Argo oxygen data bias correction

Even after delayed-mode processing and standard quality control, Argo DO profiles are known to be systematically low relative to high-quality ship-based observations. To quantify the influence of a systematic offset in delayed-mode Argo, we produced two global reconstructions using the same machine-learning framework and predictors. The first was a standard reconstruction using CTD, OSD, and delayed-mode Argo profiles. The second was the bias-corrected reconstruction, which was otherwise identical but utilized the CTD, OSD, and delayed-mode Argo values adjusted by adding 1.69 μmol kg⁻¹ to every delayed-mode Argo measurement, following Wang et al. (2025). A comparison of the two reconstructions is shown in Section [4.4.5.5](#). All the other main results of the paper are based on the bias-corrected reconstruction.

3 Model performance

3.1 Model temporal cross-validation

We conducted 8-fold temporal cross-validation on each of the six models. In each fold f , data from eight test years $\{1960 + f + 8k\}_{k=0}^7$ formed the test set, with the remaining years for training.

We trained each model using its optimized hyperparameters (Sect. 2.2.3) on the training set, predicted the DO values for the test years, and computed the mean bias (ΔDO), mean absolute error (MAE), root-mean-square error (RMSE), and coefficient of determination (R^2) on the held-out data. These metrics collectively provide a comprehensive understanding of the model’s predictive accuracy and bias. The results are presented in Tables [S3 – S6](#)~~S2–5~~.

$$RMSE = \sqrt{\frac{1}{n} \sum_{i=1}^n (y_i - \hat{y}_i)^2} \quad (813)$$

$$MAE = \frac{1}{n} \sum_{i=1}^n |y_i - \hat{y}_i| \quad (914)$$

$$R^2 = 1 - \frac{\sum_{i=1}^n (y_i - \hat{y}_i)^2}{\sum_{i=1}^n (y_i - \bar{y})^2} \quad (1015)$$

$$\Delta DO = \frac{1}{n} \sum_{i=1}^n (y_i - \hat{y}_i) \quad \Delta DO = \frac{1}{n} \sum_{i=1}^n y_i - \hat{y}_i \quad (116)$$

All six learners exhibited consistent skill across the eight temporal folds, with only minor spread in error metrics (Table S3 – S6S3-6). LightGBM displayed high stability, with MAEs varying by less than 1 $\mu\text{mol kg}^{-1}$ (10.11–11.04) and RMSEs under 1.3 $\mu\text{mol kg}^{-1}$ (16.38–17.59), yielding an R^2 range of 0.957–0.961. RF delivered the lowest RMSE (15.97–17.27) and highest R^2 (0.958–0.963). In contrast, CatBoost and Hist_GBT had slightly higher mean errors (MAEs of up to 11.04 and 11.42 and RMSEs of up to 17.57 and 17.99, respectively) and slightly greater inter-fold variability, indicating higher sensitivity to the specific training/test split (Table S3 – S6S2-5). Crucially, no model exhibited outlier folds with degraded performance, as all the models maintained MAEs < 12 $\mu\text{mol kg}^{-1}$ and $R^2 > 0.95$. This uniformity across folds confirms strong temporal generalization and validates our choice of an ensemble approach (Bergmeir & Benítez, 2012; Roberts et al., 2017).

3.2 Evaluation against independent observations

We evaluated both the ensemble and each single-individual model against an independent filtered GLODAPv2 dissolved-oxygen dataset, treated here as ground truth. Filtered GLODAPv2 profiles were averaged into the same $1^\circ \times 1^\circ$ grid and monthly time step as the reconstructions.

Table 3. Comparison of ensemble and single-individual models on the filtered GLODAPv2 dataset

Model	MAE ($\mu\text{mol kg}^{-1}$)	RMSE ($\mu\text{mol kg}^{-1}$)	R^2	ΔDO ($\mu\text{mol kg}^{-1}$)
<u>BLENDREnsemble</u>	<u>10.20410.238</u>	<u>18.13918.170</u>	<u>0.9680.967</u>	<u>-0.334-0.296</u>
<u>Equal-weight ensembleEnsemble(static weight=1)</u>	10.434	18.302	0.967	-0.214
RF	10.266	18.394	0.966	-0.531
XGBoost	12.136	19.502	0.962	0.270
ERT	11.402	19.620	0.962	-1.167
LightGBM	11.314	18.968	0.964	0.167
Hist_GBT	11.942	19.739	0.962	-0.099
CatBoost	11.549	19.275	0.963	0.431

Table 3 demonstrates the clear advantage of the BLENDR framework. A stricter sensitivity test using a wider spatiotemporal exclusion criterion yielded very similar validation metrics (Table S7), suggesting that the main evaluation results are not sensitive to the original filtering choice. While the equal-weight ensemble outperformed most individual models, its MAE was still slightly higher than that of RF. This shows that simple averaging does not always outperform the best individual model, because weaker learners can still introduce additional errors. This improved performance

408 ~~is likely related to two reasons. BLENDR used each model's cross-validation skill and further~~
409 ~~optimized the weights through the spatially coherent dynamic weighting scheme. While an equal-~~
410 ~~weight ensemble (static weight = 1) outperformed most single models, our RMSE-based dynamic~~
411 ~~weight further improved accuracy, achieving the lowest overall errors. This demonstrates that~~
412 ~~leveraging each learner's cross-validation skill yields a measurably better ensemble than equal~~
413 ~~weighting does.~~ Among the individual algorithms, the RF and LightGBM performed best, whereas
414 XGBoost and Hist_GBT performed at the lower end. All ~~the~~ models had absolute biases below
415 1.2 maintained the bias under 0.6 $\mu\text{mol kg}^{-1}$. No single individual method showed unstable or
416 extremely poor performance in this evaluation, underscoring the robustness of our dynamic
417 weighting in combining complementary strengths and minimizing weaknesses.

418 419 **3.3 Uncertainty estimations**

420 We quantified three distinct contributors to uncertainty in the reconstructed DO field, namely,
421 measurement, grid, and algorithm uncertainty. These components were estimated separately and
422 then combined to provide a first-order global uncertainty estimate.

423
424 The measurement uncertainty (ΔO_{meas}) represents the random errors of the *in situ* dissolved
425 oxygen observations. We adjusted the delayed-mode Argo DO values by adding a constant +1.69
426 $\mu\text{mol kg}^{-1}$ (Sect. 2.1.1), following the global bias assessment of Wang et al. (2025). After this bias
427 correction, we treated Argo and CTD/OSD as unbiased on average, and ΔO_{meas} represents only
428 the residual random measurement error. We assumed constant uncertainties of 1 $\mu\text{mol kg}^{-1}$ for
429 OSD and CTD and 3 $\mu\text{mol kg}^{-1}$ for Argo, following Ito et al. (2024). We then summarized a
430 representative value across all observations using the root-mean-square of these assigned
431 uncertainties.

432
433 The grid uncertainty (ΔO_{grid}) quantifies the error associated with assigning a single value to a $1^\circ \times 1^\circ$
434 grid cell. We estimated ΔO_{grid} from the dispersion of collocated observations within each grid cell.
435 For each grid cell with at least 10 collocated observations, we computed the within-cell standard
436 deviation as follows:

$$437 \quad \Delta O_{\text{grid}} = \sigma = \sqrt{\frac{1}{n-1} \sum_{i=1}^n (O_i - \bar{O})^2}$$

438 ~~(4217)~~

439 where O_i is the i -th observation in the cell and \bar{O} is the mean value of the observations. We then
440 averaged σ over all qualifying cells to obtain a single global estimate of ΔO_{grid} .

441
442 The algorithm uncertainty (ΔO_{alg}) reflects the error introduced by the machine learning
443 reconstruction process. We trained six models (RF, XGBoost, LightGBM, CatBoost, ERT, and
444 Hist_GBT) using DO observations and environmental factors. Each model was optimized via
445 Bayesian hyperparameter tuning and validated using an 8-fold cross-validation procedure, yielding
446 an MAE for each model, denoted by error_1 through error_6 . We then computed the prior weight for
447 the i -th model using an exponential decay function:

448
$$\omega_i = \frac{\exp(-error_i)}{\sum_{j=1}^6 \exp(-error_j)} \quad (1318)$$

449 and estimated the algorithm uncertainty as the weighted average of the MAE:

450
$$\Delta O_{alg} = \sum_{i=1}^6 \omega_i error_i \quad (1419)$$

451 Finally, the total uncertainty (ΔO_{total}) in the reconstructed dissolved oxygen field is expressed as
452 follows:

453
$$\Delta O_{total} = \sqrt{\Delta O_{meas}^2 + \Delta O_{grid}^2 + \Delta_{alg}^2} \quad (1520)$$

454

455 Using this framework, the estimated global component uncertainties were Δ
456 $O_{meas} = 1.60 \mu\text{mol kg}^{-1}$, $\Delta O_{grid} = 4.56 \mu\text{mol kg}^{-1}$, and $\Delta O_{alg} = 10.29 \mu\text{mol kg}^{-1}$, resulting in a
457 combined global uncertainty of $\Delta O_{total} = 11.37 \mu\text{mol kg}^{-1}$.

458

459 4 Intercomparison with existing oxygen products

460 4.1 Comparison with filtered GLODAPv2 observations

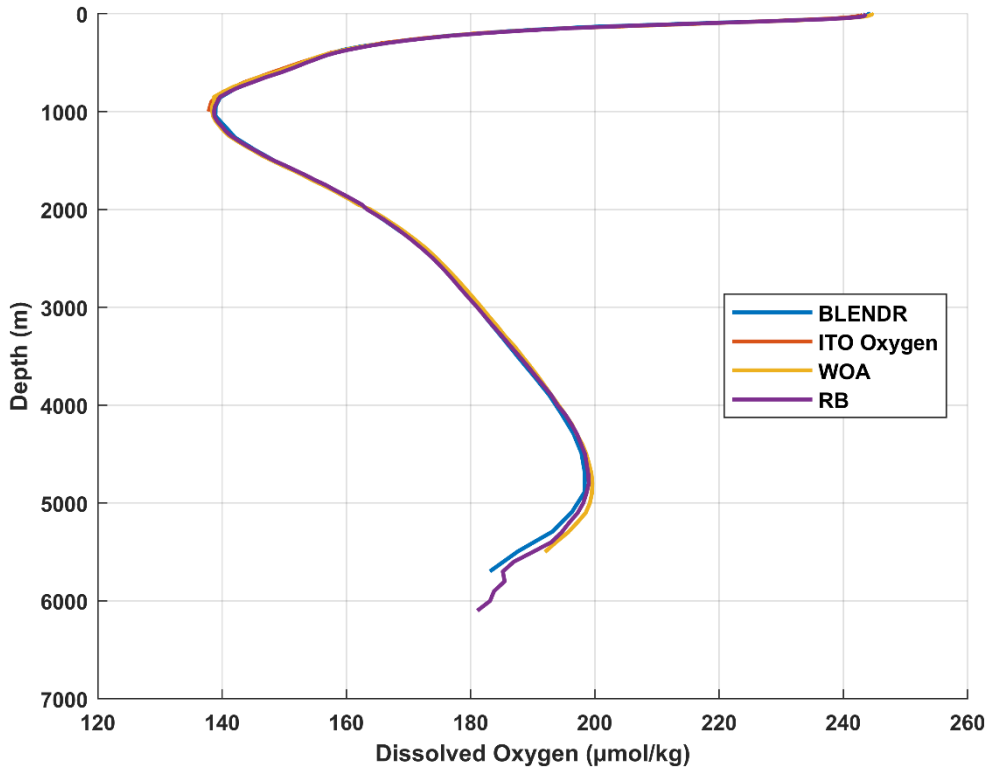
461 Compared with GOBAI (Sharp et al., 2023) and ITO (Ito et al., 2024), BLENDR showed the best
462 overall agreement with the filtered GLODAPv2 reference dataset (Table 4). The comparison was
463 conducted both over the full filtered GLODAPv2 dataset and within the coverage domains of GOBAI
464 and ITO (Table 4). BLENDR achieved the lowest MAE and RMSE and the highest R^2 among the three
465 products, with values of $10.204 \mu\text{mol kg}^{-1}$, $18.139 \mu\text{mol kg}^{-1}$, and 0.968 , respectively. Within the
466 GOBAI coverage, BLENDR had a lower RMSE and a higher R^2 than GOBAI, although its MAE was
467 slightly higher. Its mean bias was also closer to zero. Within the ITO coverage, BLENDR again
468 showed lower MAE and RMSE and a higher R^2 than ITO, although its mean bias was farther from
469 zero. Overall, these comparisons show that BLENDR compares favorably with existing products
470 both over the full filtered GLODAPv2 comparison set and within their respective coverage domains.

471 **Table 4. Performance comparison of BLENDR, GOBAI, and ITO against filtered GLODAPv2**

<u>Product</u>	<u>MAE ($\mu\text{mol kg}^{-1}$)</u>	<u>RMSE ($\mu\text{mol kg}^{-1}$)</u>	<u>R^2</u>	<u>Δ DO ($\mu\text{mol kg}^{-1}$)</u>
<u>BLENDR</u>	<u>10.204</u>	<u>18.139</u>	<u>0.968</u>	<u>-0.334</u>
<u>GOBAI on</u> <u>filtered</u> <u>GLODAPv2</u>	<u>11.101</u>	<u>19.875</u>	<u>0.956</u>	<u>-0.971</u>
<u>BLENDR in</u> <u>GOBAI</u> <u>coverage</u>	<u>11.115</u>	<u>19.658</u>	<u>0.963</u>	<u>-0.470</u>

<u>ITO on filtered</u>	<u>13.415</u>	<u>22.958</u>	<u>0.951</u>	<u>-0.123</u>
<u>GLODAPv2</u>				
<u>BLENDR in</u>	<u>11.824</u>	<u>19.966</u>	<u>0.964</u>	<u>-0.544</u>
<u>ITO coverage</u>				

472 **4.2 Comparison of mean vertical profile**

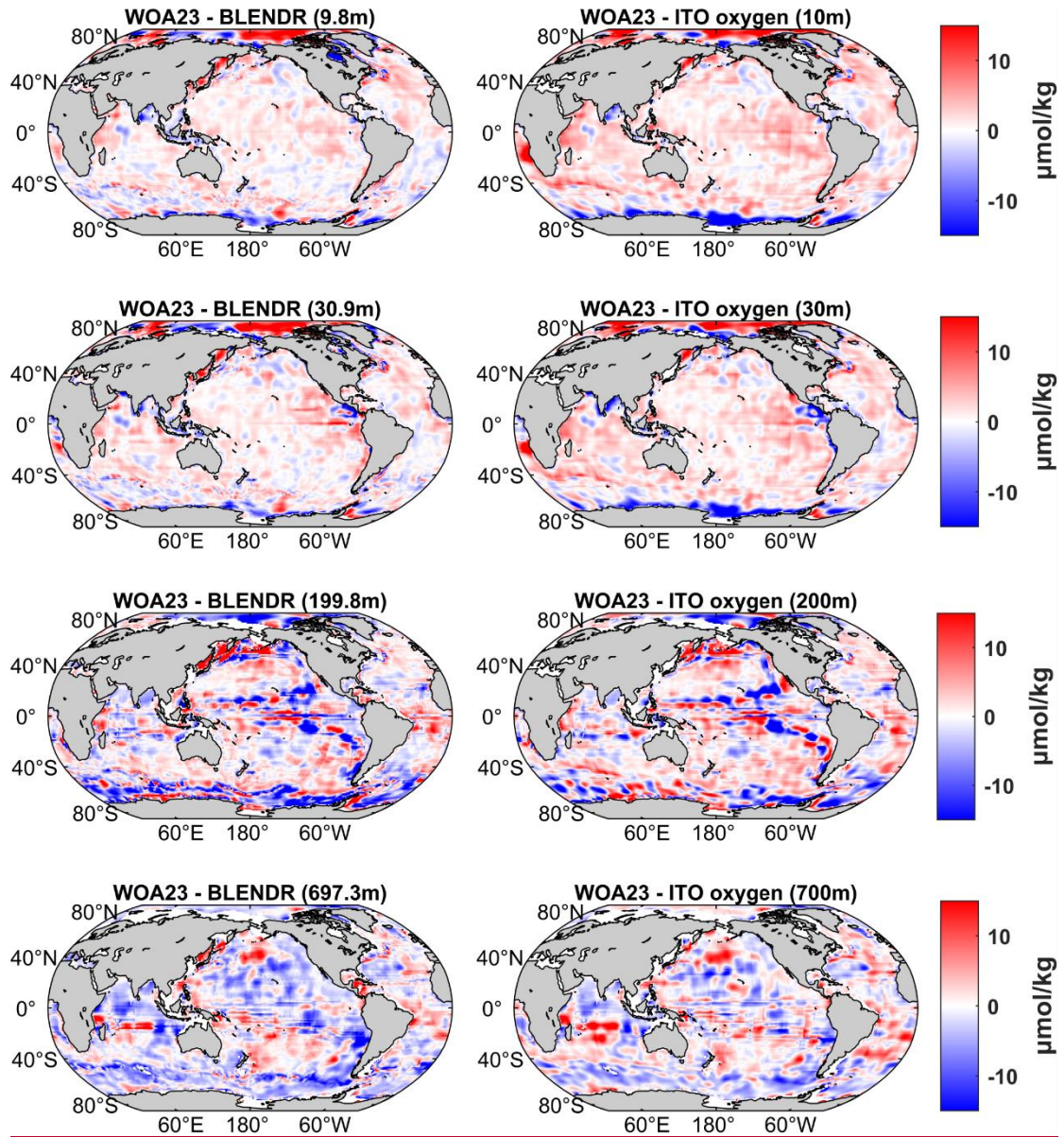


473
 474 **Figure 2. Global mean vertical profiles of different dissolved oxygen products (1965 – 2022).** Solid lines show our
 475 reconstruction (blue), Roach & Bindoff’s reconstruction (purple), ITO Oxygen (orange) and WOA23 climatology
 476 (yellow), plotted from the surface down to 6000 m.

477
 478 The global mean vertical profile of BLENDR is broadly consistent with those of ITO Oxygen, WOA23,
 479 and the DIVA-based product of Roach and Bindoff (RB) over most of the water column (Figure 2).
 480 The four profiles are very close near the surface. In the upper 0 – 1000 m, BLENDR, ITO, WOA23,
 481 and RB remain highly consistent. From about 1,000 to 3,500 m, the profiles of BLENDR, WOA23,
 482 and RB are nearly indistinguishable, indicating that BLENDR reproduces the large-scale deep-ocean
 483 oxygen structure well in this depth range. Below 3,500 m, the profile of RB remains slightly closer
 484 to WOA23, but the differences among the products are still small. Overall, the mean-profile
 485 comparison shows that BLENDR remains close to the other products over most of the water column
 486 and reproduces the large-scale vertical structure consistently.

487

4.3 Spatial difference from climatological distribution

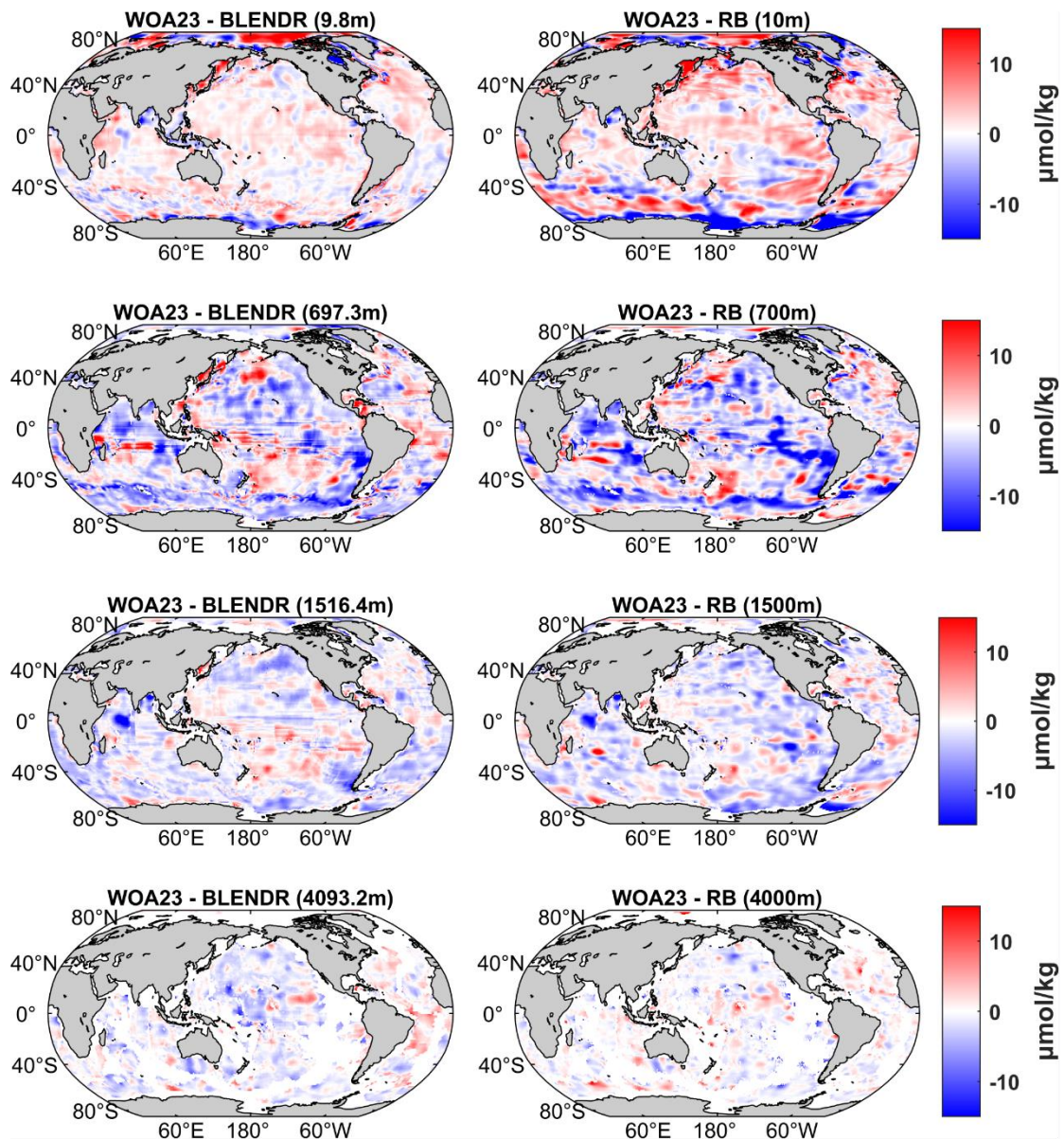


488

489 **Figure 3. Spatial differences from WOA23 at four representative depths for this study and ITO Oxygen. Left panels**

490 **show WOA23 minus this study at 9.8, 30.9, 199.8, and 697.3 m. Right panels show WOA23 minus ITO Oxygen at 10,**

491 **30, 200, and 700 m. Units are $\mu\text{mol kg}^{-1}$.**



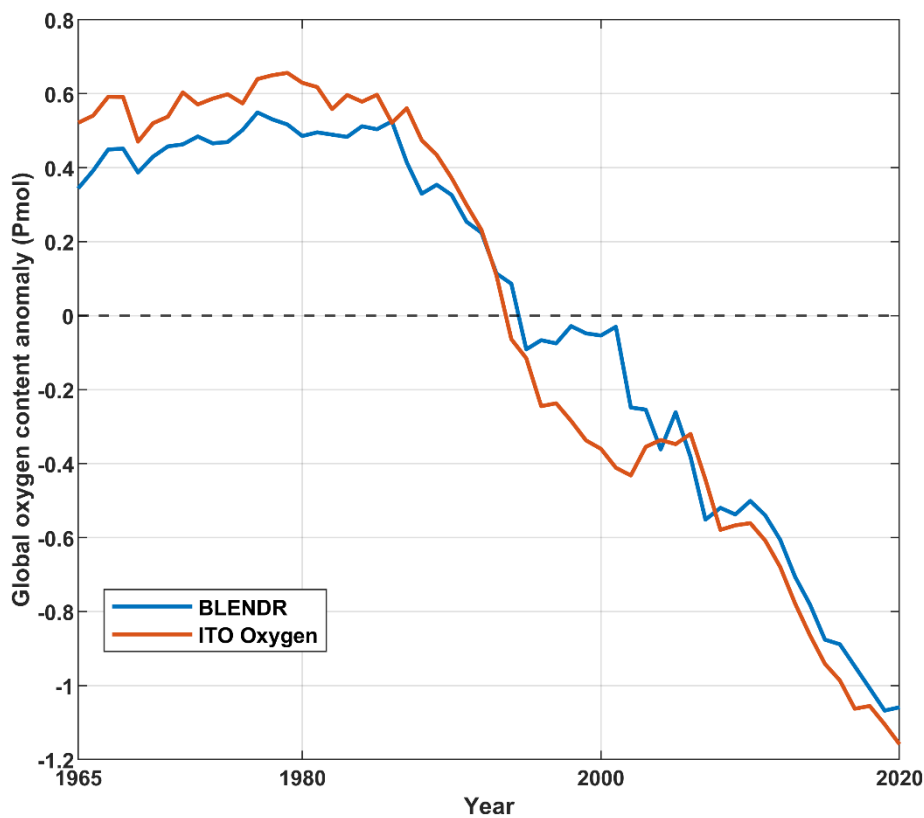
492 **Figure 4. Spatial differences from WOA23 at four representative depths for this study and the Roach and Bindoff**
 493 **(RB) product. Left panels show WOA23 minus this study at 9.8, 697.3, 1516.4, and 4093.2 m. Right panels show**
 494 **WOA23 minus RB at 10, 700, 1500, and 4000 m. Units are $\mu\text{mol kg}^{-1}$.**
 495

496
 497 Relative to WOA23, BLENDR shows smaller large-scale departures than ITO in the upper layer and
 498 broadly comparable differences to RB in the deep layer (Figures 3 and 4). Compared with ITO
 499 (Figure 3), BLENDR is closer to WOA23, particularly in the surface layer, and shows smaller
 500 differences in many low- and mid-latitude regions. At around 10 m depth, BLENDR shows small
 501 differences, generally within $\pm 2 \mu\text{mol kg}^{-1}$, except in some high-latitude regions. In comparison,
 502 ITO exhibits broader regions where it is lower than WOA23 in the subtropical gyres and more
 503 pronounced regions where it is higher than WOA23 under the Antarctic Circumpolar Current. At
 504 around 30 m, the differences in BLENDR remain small in most mid-latitude regions, with larger
 505 variability near boundary currents. In contrast, ITO again shows larger departures in the subtropics
 506 and southern high latitudes. These results indicate that BLENDR is generally closer to WOA23 in
 507 the surface ocean. At around 200 m, both BLENDR and ITO Oxygen show larger departures from

508 WOA23, reaching about $\pm 10 \mu\text{mol kg}^{-1}$ in the tropical and subtropical regions. At around 700 m,
509 BLENDR and WOA23 remain within about $\pm 8 \mu\text{mol kg}^{-1}$ over large parts of the Atlantic and Pacific
510 basins.

511 In the comparison with RB, BLENDR shows a similar reduction in differences from WOA23 with
512 increasing depth (Figure 4). At around 10 m, BLENDR is generally closer to WOA23 than RB, with
513 smaller spatial differences over much of the open ocean. At around 700 m, both BLENDR and RB
514 show relatively large differences from WOA23. At around 1500 m, the differences decrease in both
515 products, and at around 4000 m they decrease further, with both products showing generally
516 smaller differences relative to WOA23. This comparison indicates that BLENDR agrees more closely
517 with WOA23 in the surface layer, while in the deep ocean both BLENDR and RB show reduced
518 differences below about 1500 m.

519 **4.4 Comparison of oxygen content anomaly**



520
521 **Figure 5. Global oxygen content anomaly in the upper 1000 m from BLENDR and ITO Oxygen during 1965–2020.**
522 The blue line denotes BLENDR and the orange line denotes ITO Oxygen. Anomalies are expressed in Pmol relative
523 to the mean over the comparison period.

524
525 BLENDR and ITO Oxygen show a similar multidecadal evolution of upper-ocean oxygen content
526 anomaly during 1965 - 2020 (Figure 5), with positive anomalies before the early 1990s, a rapid
527 decline during the 1990s, and persistent negative anomalies after 2000. ITO Oxygen exhibits
528 slightly larger anomaly amplitudes than BLENDR in the earlier part of the record, but the long-term
529 downward trend and the timing of the transition from positive to negative anomalies are similar in
530 both products. This result indicates that BLENDR is consistent with ITO Oxygen in capturing the
531 large-scale decline of upper-ocean oxygen content.

4.5 Global ocean DO distribution and trends

4.5.1 Spatial distributions along the vertical direction

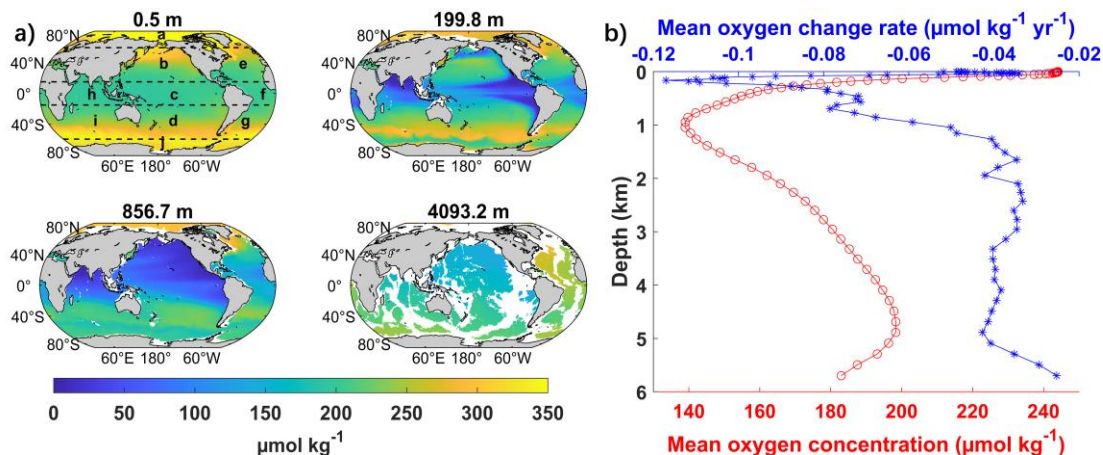


Figure 16. Global distribution and vertical structure of dissolved oxygen. (a) Climatological mean dissolved oxygen concentration at four representative depths (0.5 m, 199.8 m, 856.7 m, and 4,093.2 m) from the reconstructed global product. Letters indicate the ten regions: a) Arctic Ocean (AO), b) North Pacific (NP), c) Equatorial Pacific (EP), d) South Pacific (SP), e) North Atlantic (NA), f) Equatorial Atlantic (EA), g) South Atlantic (SA), h) Equatorial Indian (EI), i) South Indian (SI), and j) Southern Ocean (SO). This regionalization scheme is adopted from Schmidtke et al. (2017). (b) Global mean vertical profiles of the dissolved oxygen concentration (red; $\mu\text{mol kg}^{-1}$) and its long-term linear change rate (blue; $\mu\text{mol kg}^{-1} \text{yr}^{-1}$).

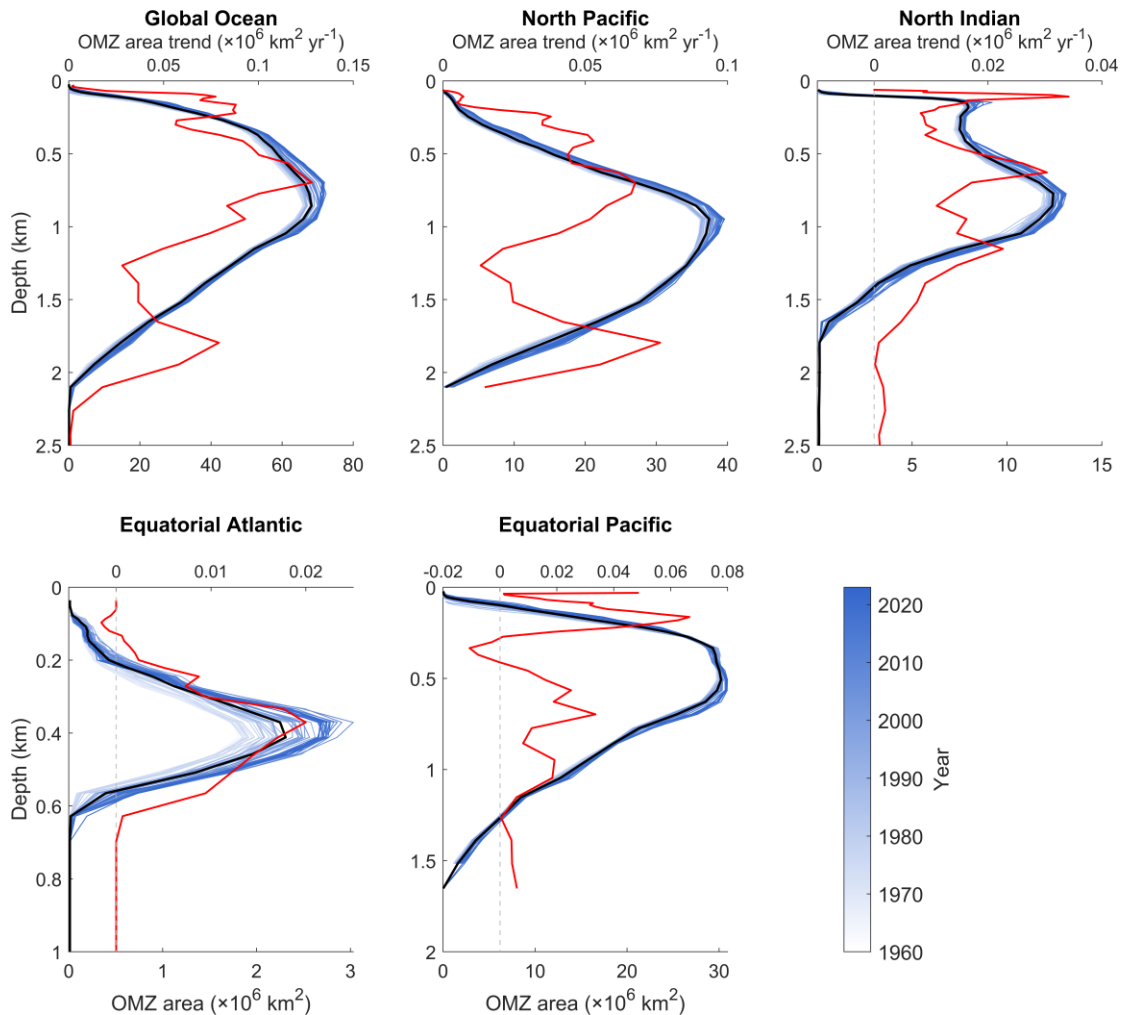
Our reconstruction shows the full vertical extent of historical deoxygenation from the surface ocean to the abyss, providing continuous monthly fields down to 5,902 m (Figure 1a6a). The surface layer (0.5 m) is generally characterized by high DO concentrations, reflecting air–sea exchange and photosynthetic production (Ryther, 1956; Kolber et al., 2000). The especially high values at high latitudes ($> 300 \mu\text{mol kg}^{-1}$) are consistent with enhanced oxygen solubility in colder waters. At approximately 200 m, strong horizontal contrasts emerge, with broad low-oxygen regions in the eastern tropical Pacific and northern Indian Ocean ($< 160 \mu\text{mol kg}^{-1}$), while subpolar regions remain relatively oxygenated ($> 200 \mu\text{mol kg}^{-1}$). This rapid decrease reflects diminished gas exchange and ongoing microbial respiration (Keeling et al., 2010; Schmidtke et al., 2017). At approximately 850 m, the lowest DO concentrations are most evident, with the concentrations in the eastern Pacific and northern Indian Ocean decreasing below $150 \mu\text{mol kg}^{-1}$, whereas the North Atlantic (NA) mid-depth ocean maintains higher concentrations ($180\text{--}200 \mu\text{mol kg}^{-1}$). In the bathypelagic zone ($\sim 4,000$ m), DO becomes spatially uniform ($180\text{--}200 \mu\text{mol kg}^{-1}$) across basins, which is consistent with the large-scale deep-water mass structure (Talley, 2013). Overall, along the water column, the DO concentration peaks at the surface and reaches a local minimum of approximately $139 \mu\text{mol kg}^{-1}$ near the classical OMZ at approximately 1,000 m but then slowly increases toward $200 \mu\text{mol kg}^{-1}$ at approximately 4,500 m (Figure 1b6b).

The global mean DO trend from 1960 to 2023 was negative at nearly all depths, with the strongest deoxygenation in the subsurface ocean and weaker trends in the surface and deep ocean (Figure 1b6b). While the deoxygenation rate was low ($-0.04 \mu\text{mol kg}^{-1} \text{yr}^{-1}$) at the surface, the decline

565 accelerated greatly below 60 m, reaching its most negative values between 150 and 200 m (-0.12
 566 $\mu\text{mol kg}^{-1} \text{yr}^{-1}$). This pattern reflects an amplification of shallow subsurface oxygen loss, most likely
 567 driven by stronger stratification that inhibits ventilation exchange and by increased microbial
 568 respiration (Keeling et al., 2010; Schmidtko et al., 2017).

569

570 **4.5.2 Depth-basin patterns in the OMZ area**



571

572 **Figure 27. Vertical evolution of the OMZ area across major ocean basins during 1960–2023.** Vertical profiles of
 573 the annual OMZ area (blue lines; threshold = $60 \mu\text{mol kg}^{-1}$) for the global ocean and four major basins: North Pacific,
 574 North Indian, Equatorial Atlantic, and Equatorial Pacific. Individual blue curves represent yearly OMZ area profiles,
 575 with color shading indicating the year (1960–2023). The black curves show the long-term mean OMZ area at each
 576 depth. The red curves denote the linear trend in the OMZ area with depth ($\times 10^6 \text{ km}^2 \text{ yr}^{-1}$), highlighting the depth-
 577 dependent expansion or contraction of low-oxygen waters. Here, the North Indian corresponds to the Equatorial
 578 Indian (EI) in Figure 1 together with the Bay of Bengal and Arabian Sea. Here, the North Indian includes the
 579 Equatorial Indian labeled h in Figure 6a, together with the Bay of Bengal and Arabian Sea.

580

581 Over the past six decades, the OMZ ($\text{DO} < 60 \mu\text{mol kg}^{-1}$) has existed primarily at depths between
 582 100 m and 2,000 m, but its vertical structure and magnitude vary strongly between basins (Figure
 583 27). In the global mean profile, the total OMZ area increases from the surface to a broad maximum
 584 near 800 m and then decreases toward deeper waters. In the North Pacific (NP), the OMZ is thickest,

585 with a wide band of large area between approximately 800 and 1,200 m, which is consistent with
586 slow intermediate-water ventilation and long residence times that allow for respiration to consume
587 oxygen (Karstensen et al., 2008; Paulmier and Ruiz-Pino, 2009). In the North Indian (NI), by contrast,
588 the largest OMZ area is much shallower, between approximately 100 and 1,000 m, reflecting a
589 combination of weak thermocline ventilation and strong export production in the Arabian Sea and
590 Bay of Bengal that produces very intense hypoxia (Naqvi et al., 2006; Keeling et al., 2010). The
591 Equatorial Pacific (EP) and Equatorial Atlantic (EA) have thinner OMZ layers centered at
592 approximately 300–600 m. The OMZ in the EP is located primarily in the eastern ocean because of
593 relatively stagnant cyclonic gyres north and south of the equator in the east subsurface layers,
594 which are poorly ventilated (Keeling et al., 2010). In the Atlantic, the OMZ area is much smaller
595 than that in the Pacific, which is consistent with stronger ventilation of the Atlantic thermocline
596 and intermediate waters (Stramma et al., 2008; Talley et al., 2013).

597

598 These basin differences are also reflected in the vertical profiles of the OMZ extent. OMZ extents
599 have distinct depth profiles across the regions: the NP, EP, and EA are characterized by a single local
600 maximum, whereas the North Indian Ocean (including the Arabian Sea and Bay of Bengal) exhibits
601 two local maxima, suggesting periodic intrusions of oxygen-rich water (Jain et al., 2017; Schmidt et
602 al., 2019; Sarma and Udaya Bhaskar, 2018). The high productivity in the western Arabian Sea region
603 leads to increased oxygen consumption (Acharya and Panigrahi, 2016), whereas the oxygen-rich
604 Somali Current, approximately 500 m deep, introduces oxygen, particularly during summer (Zhang
605 et al., 2022), resulting in weaker OMZs at this depth. Persian Gulf Water (PGW) in the Bay of Bengal
606 contributes to a modest increase in oxygen at 350–450 m (Jain et al., 2017), resulting in a reduced
607 OMZ. These intrusions disrupt the continuity of OMZs, leading to the dual-minima pattern
608 observed in these regions. This phenomenon highlights the complex and dynamic nature of OMZ
609 distribution and its susceptibility to various oceanographic processes.

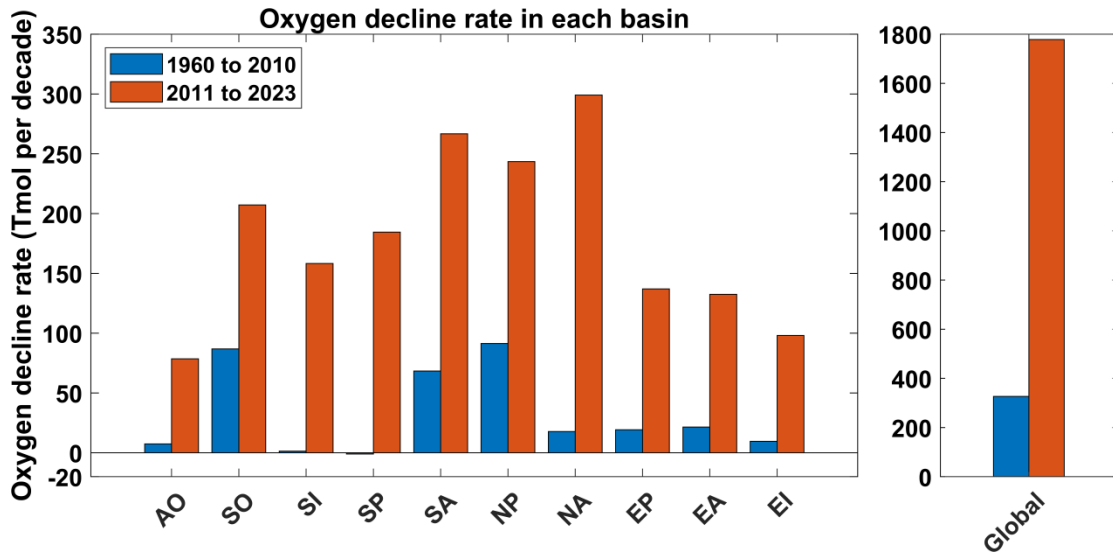
610

611 Over the 1960–2023 period, the OMZ area profile gradually expanded across nearly all depths in
612 terms of the global mean and most basins (Figure 27). These changes indicate a significant shift in
613 the vertical distribution and extent of low-oxygen seawater globally over the past six decades.
614 Specifically, the global OMZ extent growth rate was highest at 400–1,000 m because of expansion
615 across all regions, with its peak at 600–700 m due to expansion in the EP and NP. Therefore, while
616 the largest OMZ extent was approximately 900 m, shifts to the much shallower 600–700 m layer
617 are likely in the future. After this peak, the horizontal expansion rate of the OMZ decreased, with
618 the lowest rates occurring at 1,300–1,600 m. However, the expansion rates increased again beyond
619 1,600 m because of expansion-growth in the NP.

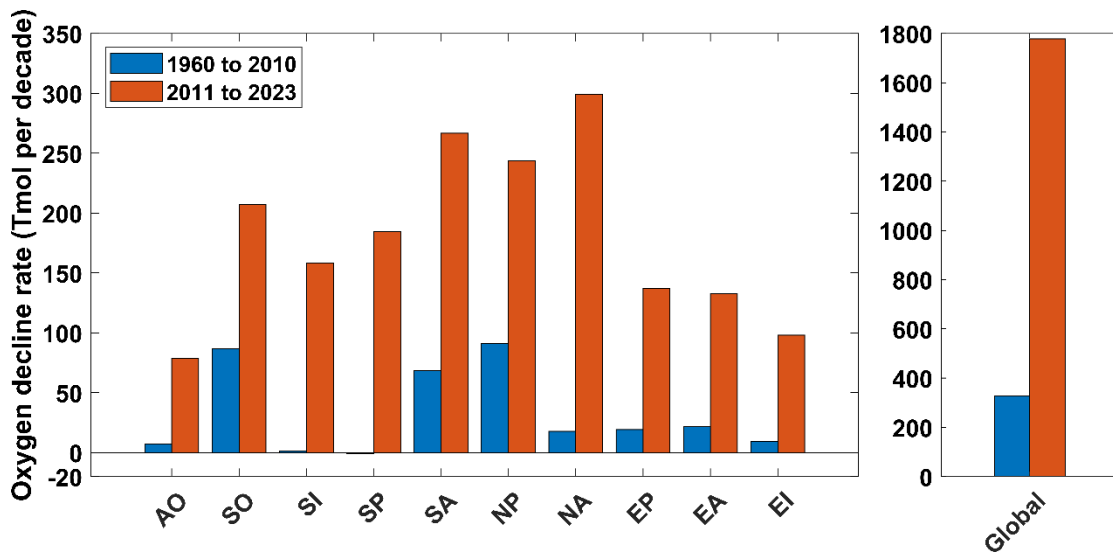
620

621 **45.3 Basin-scale deoxygenation and spatial trend pattern oxygen content and deoxygenation**
622 **rates**

623



624



625

626 **Figure 38. Decline in oxygen rates across major ocean basins.** Decadal oxygen decline rates are shown for ten
 627 individual ocean basins and for the global ocean and were estimated separately for 1960–2010 (blue) and 2011–
 628 2023 (orange).

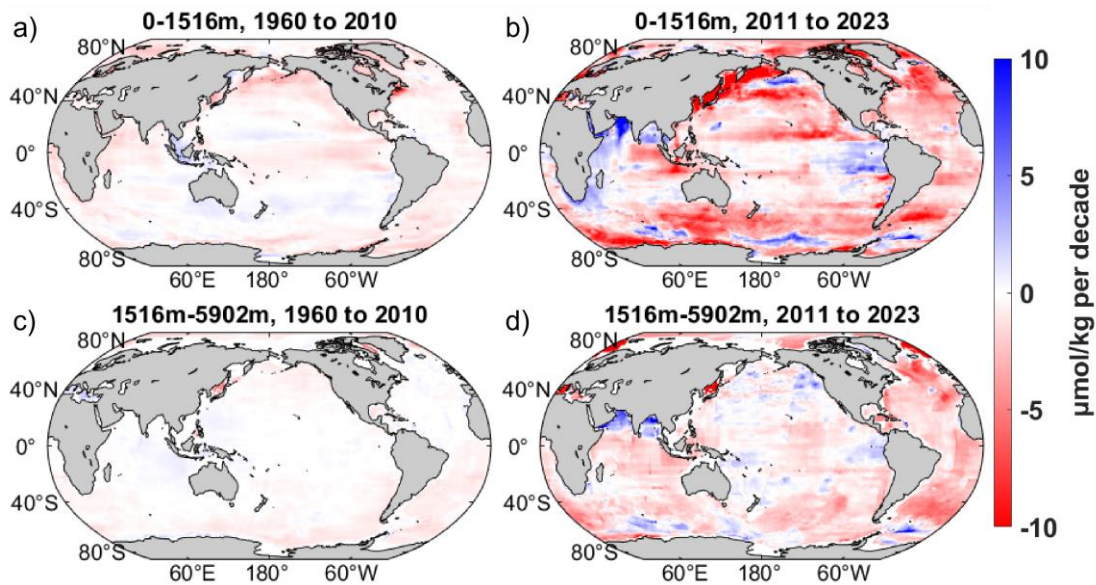
629

630 Deoxygenation was more negative after 2010 across all major ocean basins, indicating stronger
 631 recent oxygen loss over the 1960–2023 record (Figure 38). During the period from 1960 to 2010,
 632 the deoxygenation rates were generally modest. The greatest loss (91.4 ± 17.7 Tmol decade⁻¹)
 633 occurred in the NP, followed by the Southern Ocean (SO) (86.8 ± 10.5 Tmol decade⁻¹) and South
 634 Atlantic (SA) (68.3 ± 10.4 Tmol decade⁻¹). In the Southern Indian (SI) and South Pacific (SP) basins,
 635 the deoxygenation trends from 1960 to 2010 were almost negligible. This likely reflects the much
 636 sparser observational coverage is highly likely due to insufficient measurements in the Southern
 637 Hemisphere during the early record than during the Argo era. in the early record relative to those
 638 in the Argo era.

639

640 In the period after 2010, oxygen loss trends significantly increased across all the basins. The NA
 641 loss increased by more than a factor of 16 to 299.1 ± 45.8 Tmol decade⁻¹. The SA and NP both

642 exceeded $240 \text{ Tmol decade}^{-1}$. The Arctic Ocean (AO) accelerated from near zero to 78.6 ± 18.1
643 Tmol decade^{-1} . This recent acceleration of oxygen loss is attributed to amplified warming of Atlantic
644 inflow from the 2000s to the 2010s, which reduces oxygen solubility and advects low-oxygen
645 waters into the basin (Wu et al., 2025).



646

647 **Figure 9. Spatial distribution of dissolved oxygen trends for the upper layer (0 – 1,516 m) and deep layer (1,516 –**
648 **5,902 m) during 1960 – 2010 and 2011 – 2023.** Panels (a) and (b) show the upper-layer trends for 1960 – 2010 and
649 2011 – 2023, respectively, and panels (c) and (d) show the corresponding deep-layer trends. Trends are expressed
650 in $\mu\text{mol kg}^{-1}$ per decade. Positive values indicate oxygen increase, and negative values indicate oxygen decrease.

651

652 The spatial distribution of dissolved oxygen trends during 2011 – 2023 shows widespread
653 deoxygenation in both the upper layer (0 – 1,516 m) and the deep layer (1,516 – 5,902 m), with
654 the upper layer exhibiting stronger magnitudes and greater spatial heterogeneity (Figure 9).
655 Compared with 1960 – 2010, the 2011 – 2023 period exhibits much stronger and more spatially
656 heterogeneous linear trend patterns in both layers, whereas the earlier period is characterized by
657 weaker and more spatially uniform changes.

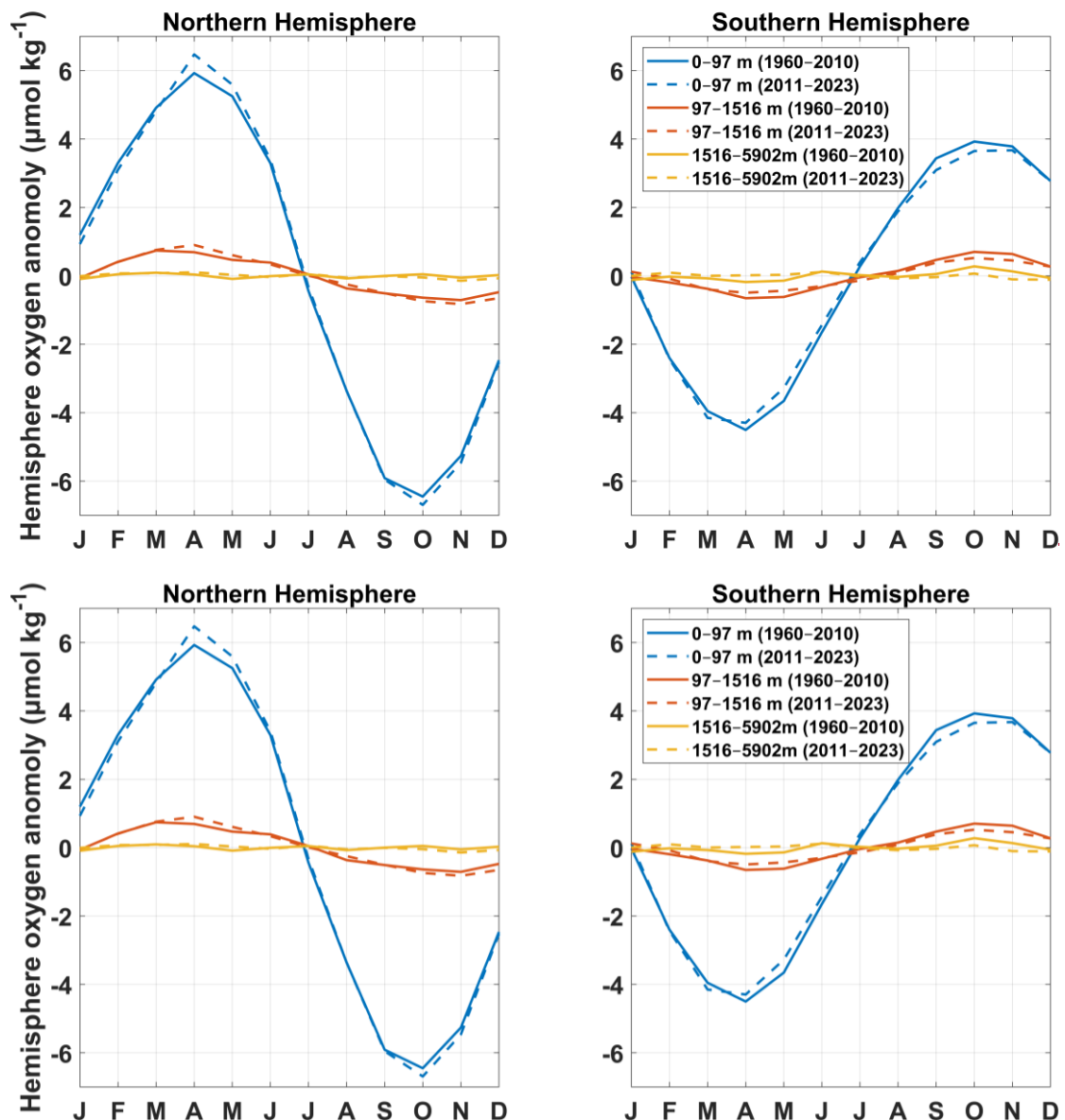
658

659 Although negative trends dominate much of the Pacific, Atlantic, and Southern oceans during
660 2011 – 2023, several spatially confined regions of positive trends are also evident. These include
661 the eastern equatorial Pacific (Espinoza-Morriberón et al., 2019), the Southern Ocean (Iida et al.,
662 2013; Morrison et al., 2022), and the North Indian Ocean (Narvekar et al., 2025; Nayak et al., 2025).
663 Some of these localized increases may reflect interannual to decadal variability over the short
664 2011 – 2023 period rather than persistent long-term change. These spatial patterns are
665 nevertheless broadly consistent with previous regional studies linking oxygen increases to
666 variability in circulation, ventilation, mixing, and oxygen supply (Karstensen et al., 2008; Espinoza-
667 Morriberón et al., 2019; Busecke et al., 2019; Duteil et al., 2021; Morrison et al., 2022; Narvekar et
668 al., 2025; Nayak et al., 2025). Overall, deoxygenation remains the dominant large-scale signal
669 during 2011 – 2023, while regional oxygen increases are confined to a few dynamically distinct
670 areas.

671

672 **45.4 Hemispheric seasonal variability in dissolved oxygen**

Climatological seasonal cycle: 1960–2010 vs 2011–2023



673

674

675 **Figure 410. Climatological seasonal cycle of hemispheric mean dissolved-oxygen anomalies.** The left panel shows
 676 the Northern Hemisphere and the right panel shows the Southern Hemisphere. The blue lines denote the surface
 677 layer (0–97 m), the red lines denote the thermocline and intermediate layer (97–1,516 m), and the yellow lines
 678 denote the deep ocean (1,516–5,902 m). The solid lines represent anomalies from 1960 to 2010, and the dashed
 679 lines represent anomalies from 2011 to 2023.

680

681 Along the water column, the seasonal amplitude was strongest in the surface layer, which responds
 682 rapidly to the seasonal changes in air–sea gas exchange, surface heating and cooling, and
 683 biologically driven production and respiration. In contrast, the seasonal cycles in the thermocline
 684 and intermediate ocean (~100–1,500 m) were substantially weaker, with anomalies typically ± 1
 685 $\mu\text{mol kg}^{-1}$, and those in the deep ocean (> 1,500 m) were nearly constant throughout the year, with
 686 amplitudes below $0.1 \mu\text{mol kg}^{-1}$ (Figure 410). This rapid vertical decline in seasonality is consistent
 687 with the dominant control mechanisms in the ocean interior. Away from the surface, oxygen is

688 mainly controlled by the ventilation of intermediate waters and by the slow remineralization of
 689 sinking organic matter. These processes evolve on multiyear to decadal time scales; thus, these
 690 water masses respond weakly to the seasonal cycle (Keeling et al., 2010; Talley, 2013). At abyssal
 691 depths, water masses are ventilated in high-latitude formation regions and subsequently spread
 692 via slow interior circulation; thus, oxygen variability is controlled mainly by large-scale and long-
 693 term transport changes (Oschlies et al., 2018).

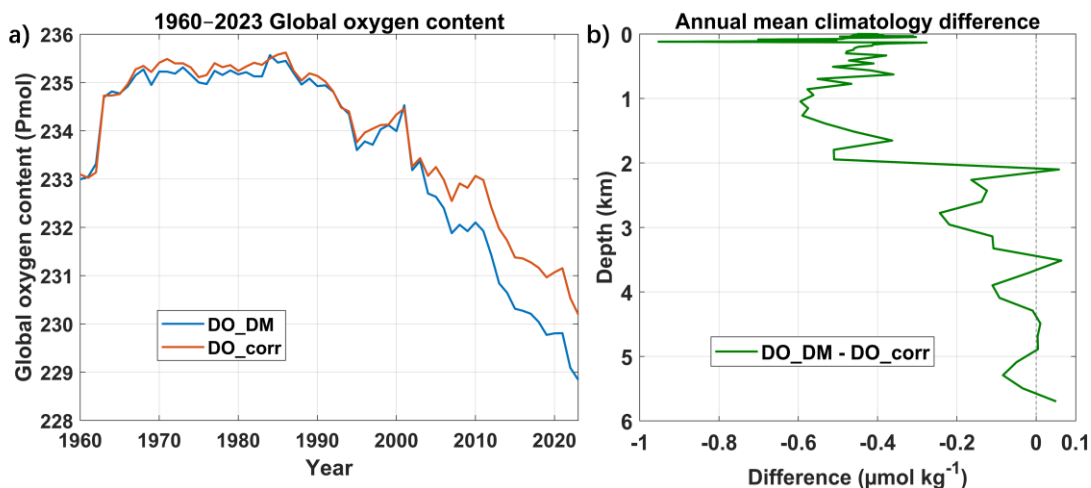
694

695 Comparing 1960–2010 with 2011–2023, the NH surface DO amplitude intensified, whereas the SH
 696 weakened. This hemispheric contrast is consistent with the direct dependence of oxygen on
 697 temperature and with the positive correlation between changes in the seasonal amplitude of
 698 surface DO and SST (Figure S3S4). In recent decades, the sea surface temperature (SST) seasonal
 699 amplitudes in large parts of the Northern Hemisphere have increased, whereas in the Southern
 700 Ocean, the SST seasonal cycle has shown robust weakening since the 1950s (Figure S4S5). Upper-
 701 ocean temperature seasonal amplitudes generally increased in the AO and other northern basins
 702 but weakened in the Southern Ocean. This pattern is consistent with the opposing NH–SH changes
 703 in DO seasonality from our reconstruction.

704 The Northern Hemisphere (NH) displays a larger seasonal amplitude than the Southern
 705 Hemisphere (SH), with peak anomalies in the surface and mid-layer ocean approximately 50%
 706 greater. A main contributor is the larger NH seasonal temperature range than the SH, which
 707 amplifies the seasonal cycle of oxygen solubility and therefore the seasonal cycle of oxygen
 708 saturation capacity (Figure S4S5). Biological processes further enhance these differences. Satellite
 709 chlorophyll-a climatology indicates that the seasonal amplitude of phytoplankton biomass is
 710 generally larger at mid- and high northern latitudes than at corresponding southern latitudes (Mao
 711 et al., 2020), consistent with a stronger seasonal DO response in the NH. Phytoplankton blooms
 712 can drive transient surface DO supersaturation in spring, whereas warmer summer conditions can
 713 increase heterotrophic respiration (Frajka-Williams et al., 2009; Carstensen et al., 2014). Argo-
 714 based analyses show that, although both hemispheres exhibit enhanced upper-ocean stratification
 715 in their respective summer seasons, the NH typically shows stronger stratification maxima than the
 716 SH (Roch et al., 2023), which limits resupply and intensifies late-summer and early-fall DO
 717 minimum (Rippeth et al., 2024).

718

719 **45.5 Effect of Argo bias correction on the reconstructed oxygen estimates**



720

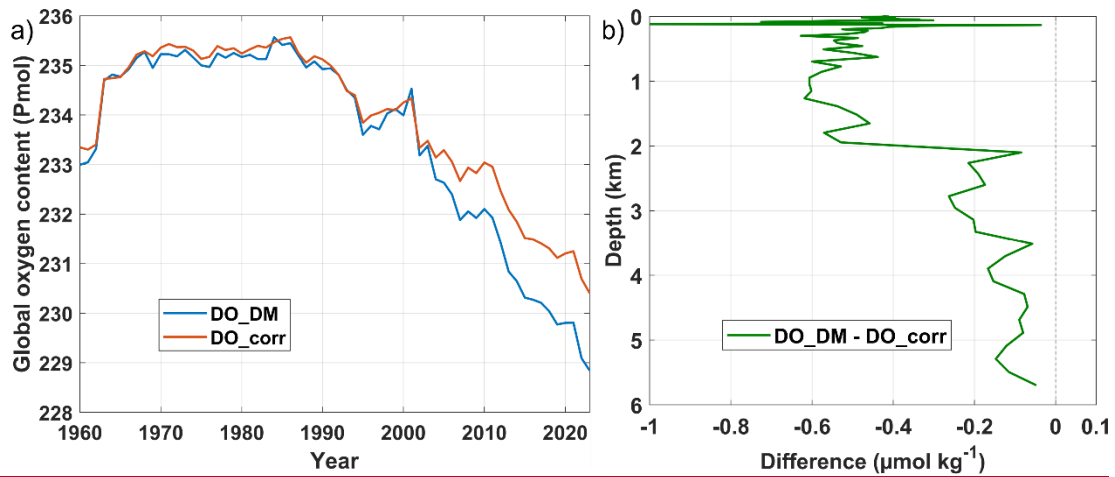


Figure 511. Comparison of global ocean oxygen content and annual mean climatology with and without Argo DO bias correction. (a) Time series of globally integrated ocean oxygen content from 1960 to 2023 based on two reconstructions that use the same machine-learning framework applied to observational oxygen profiles. The blue curve (DO_DM) used oxygen measurements from the CTD, OSD, and delayed-mode Argo profiles. The red curve (DO_corr) used the same inputs but applied a $+1.69 \mu\text{mol kg}^{-1}$ bias correction to all the Argo DO profiles following Wang et al. (2025). (b) Annual mean vertical profile of the difference between the two reconstructions (DO_DM - DO_corr).

The global time series from 1960 to 2023 confirms a long-term and large-scale decline in total dissolved oxygen content (Figure 5a11a). Over the full analysis period, both our standard and bias-corrected reconstruction methods indicate a persistent decline, with total losses of $5.4 \pm 0.5 \text{ Pmol}$ and $4.1 \pm 0.4 \text{ Pmol}$, respectively. This corresponds to overall decreases of $2.3 \pm 0.2\%$ and $1.8 \pm 0.2\%$, respectively. This magnitude of loss is consistent with prior synthesis estimates of historical deoxygenation, such as approximately $4.8 \pm 2.1 \text{ Pmol}$ of oxygen loss since 1960 by Schmidtko et al. (2017) and an overall $\sim 2\%$ decrease in oxygen in the late 20th century by Helm et al. (2011).

The Argo bias correction produces only modest changes in the reconstructed oxygen fields and does not substantially affect the long-term deoxygenation rates (Figure 5a11a). Both the standard and the bias-corrected reconstructions strongly agree prior to 2005, when the observations are constrained mainly by ship-based CTD and OSD measurements. After 2005, when the Argo observations became a significant contributor, the reconstruction that incorporates bias-corrected Argo data yielded a slightly higher global mean oxygen content than the uncorrected version did. Consequently, the bias-corrected reconstruction showed a greater global oxygen content in recent years. Vertically, the greatest differences occurred above 2,000 m, where the difference mostly ranged from -0.4 to $-0.6 \mu\text{mol kg}^{-1}$ (Figure 5b11b), due to dense Argo float sampling and strong optode biases at this depth. Beyond 2,000 m, where sampling mainly comprised sparse ship-based measurements, the difference decreased to $-0.2 \mu\text{mol kg}^{-1}$, and below approximately 3,500 m, the two reconstructions were almost indistinguishable. In summary, the Argo bias correction improves cross-platform consistency but has only a limited influence on global and basin-scale conclusions drawn from the reconstruction.

5.6 Conclusion and discussion

753 Our study generated ~~the first~~ global $1^\circ \times 1^\circ$ monthly DO dataset from 1960 to 2023, which
754 extends to 5,902 m, achieved through the BLENDR framework. BLENDR integrates six tree-based
755 learners: Random Forest, XGBoost, LightGBM, CatBoost, ERT and Hist_GBT. These models are
756 optimized using Bayesian optimization and combined via a spatially coherent dynamic weighting
757 scheme. Our ensemble moves well beyond simpler blends and applies a weighting scheme that
758 combines global prior model skill with locally constrained error information, while propagating
759 local weights through Gaussian kernel smoothing and shrinking them toward the prior weights as
760 observational support decreases.~~dynamic weighting. Our ensemble moves well beyond simpler~~
761 ~~blends and applies soft weighting that combines each model's global cross-validation skill with~~
762 ~~local error performance, allowing for the best-performing learner to dominate regionally and~~
763 ~~depthwise while downweighting those with larger local biases.~~ As a result, our reconstruction
764 achieved lower MAEs and RMSEs than those of any single-individual model or static-weight
765 blend~~equal-weight ensemble~~ on the independent filtered GLODAPv2 dataset and reproduces the
766 large-scale vertical and seasonal structure, including sharp oxycline features and deep ocean
767 signals.

768 The vertical deoxygenation profile revealed accelerating oxygen loss between 150 and 200 m at
769 rates of approximately $-0.12 \mu\text{mol kg}^{-1} \text{yr}^{-1}$, whereas surface decreases remained modest (-0.04
770 $\mu\text{mol kg}^{-1} \text{yr}^{-1}$). Consistent with this, the OMZ area expanded at nearly all depths, with the strongest
771 growth occurring between approximately 400 and 1,000 m and a maximum near 600–700 m, which
772 is driven largely by the Equatorial and North Pacific OMZs, whereas weaker yet still positive trends
773 occurred in the deeper North Pacific below 1,600 m. Since 2010, basin-scale trends have
774 accelerated strongly, particularly in the NA and AO, and most other basins have transitioned from
775 weak or negligible trends to substantial oxygen loss, which is consistent with observations of rising
776 temperature, strengthening stratification (Matear et al., 2003; Solomon et al., 2021) and with the
777 deoxygenation of Atlantic inflow feeding the AO (Wu et al., 2025). In the Southern Indian and South
778 Pacific basins, deoxygenation remained weak or even locally positive from 1960 to 2010 (Stramma
779 et al., 2010) but intensified sharply from 2011 to 2023, indicating that these basins shifted from
780 relatively stable oxygen conditions to rapid loss in step with recent upper-ocean warming and
781 circulation changes (Schmidtko et al., 2017; Oschlies et al., 2018).

782 Our analysis of hemispheric DO seasonality revealed that the Northern Hemisphere exhibits
783 seasonal peak anomalies that are approximately 50% greater than those in the Southern
784 Hemisphere in both the surface and thermocline layers. This asymmetry arises primarily from the
785 greater seasonal cycle of upper-ocean temperature in the Northern Hemisphere, which amplifies
786 the seasonal cycle of oxygen solubility, while biological and physical processes further sharpen the
787 extremes: spring phytoplankton blooms drive transient surface supersaturation, and warmer, more
788 strongly stratified summer conditions favor heterotrophic respiration and the development of late-
789 summer to early-fall oxygen minima (Frajka-Williams et al., 2009; Carstensen et al., 2014; Rippeth
790 et al., 2024).

791 A further contribution of this work is the explicit assessment of how Argo oxygen biases propagate
792 into machine-learning reconstructions. By training two parallel ensembles, one using delayed-
793 mode Argo DO together with CTD/OSD profiles (DO_DM) and the other applying a uniform $+1.69$
794 $\mu\text{mol kg}^{-1}$ correction to all Argo DO profiles (DO_corr), we directly quantified the sensitivity of
795 global oxygen inventories and trends to this widely used bias adjustment. This comparison
796 highlights that the recent correction in delayed-mode Argo does not significantly affect the

797 deoxygenation trend in global and regional oceans, which enhances the reliability of long-term,
798 observation-constrained reconstructions.

799 We note several limitations and avenues for improvement. The $1^\circ \times 1^\circ$ grid smooths small-
800 scale features such as narrow boundary currents. In addition, although ORAS5 provides
801 dynamically consistent physical predictor fields for the reconstruction, uncertainties in its
802 temperature, salinity, and circulation fields can still propagate into the reconstructed dissolved
803 oxygen through the learned relationships between physical predictors and oxygen. This issue is
804 likely more important in the deep ocean, where direct oxygen observations become much sparser
805 below 2,000 m and the reconstruction depends more strongly on the large-scale structure
806 represented by the predictor fields. Because all six models share the same ORAS5 inputs, this
807 source of uncertainty is partly structural and cannot be fully reduced by ensemble weighting. Our
808 current uncertainty estimate does not include predictor uncertainty from ORAS5 and may
809 therefore underestimate total uncertainty in poorly observed deep-ocean regions. Even after a
810 constant bias correction was applied to delayed-mode Argo oxygen, residual sensor biases and
811 calibration uncertainties in biogeochemical Argo (BGC-Argo) profiles still propagated into our
812 training data, especially around steep oxyclines (Bittig et al., 2017; Bittig et al., 2018; Gouretski et
813 al., 2024). Future work should incorporate more precisely calibrated Argo data, finer regional grids,
814 and uncertainty propagation from physical predictor fields. ~~and finer regional grids.~~

815 Overall, our dataset offers a unified, long-term view of ocean deoxygenation from the surface to
816 the abyss and, by extending coverage into the bathypelagic realm, fills a critical observational void
817 that enables studies of deep-ocean oxygen dynamics. Packaging in NetCDF with documented
818 uncertainties provides a benchmark for Earth system models and a foundation for impact studies
819 on marine habitats and biogeochemical cycles and invites the community to explore trends,
820 calibrate models and guide policies on ocean health under climate change.

821

822 **Data Availability**

823 The reconstructed global monthly dissolved oxygen dataset produced in this study is publicly
824 available in NetCDF format via Zenodo at <https://doi.org/10.5281/zenodo.19705526> (Han and
825 Zhou, 2026) ~~<https://doi.org/10.5281/zenodo.17548659>~~ (Han and Zhou, 2025) under a Creative
826 Commons Attribution 4.0 license. Source DO profile observations were obtained from the
827 International Argo Program and the national programs that contribute to Argo
828 (<https://argo.ucsd.edu>), the World Ocean Database 2023 (WOD) maintained by the U.S. National
829 Oceanic and Atmospheric Administration (NOAA; [https://www.ncei.noaa.gov/products/world-](https://www.ncei.noaa.gov/products/world-ocean-database)
830 [ocean-database](https://www.ncei.noaa.gov/products/world-ocean-database)), and the Global Ocean Data Analysis Project v2.2023 (GLODAPv2;
831 [https://www.ncei.noaa.gov/access/ocean-carbon-acidification-data-](https://www.ncei.noaa.gov/access/ocean-carbon-acidification-data-system/oceans/GLODAPv2_2023)
832 [system/oceans/GLODAPv2_2023](https://www.ncei.noaa.gov/access/ocean-carbon-acidification-data-system/oceans/GLODAPv2_2023)). Environmental predictor fields were drawn from the ORAS5
833 ocean reanalysis provided by the European Centre for Medium-Range Weather Forecasts (ECMWF;
834 <https://cds.climate.copernicus.eu/datasets/reanalysis-oras5>).

835

836

837

838 **Acknowledgments**

839 This research was supported by the National Natural Science Foundation of China (~~42341201,~~
840 42276201), and the National Key Research and Development Program of China (2023YFF0805004).
841 The authors also thank the International Argo Program and the national programs for providing
842 Argo data (<https://argo.ucsd.edu>), the National Oceanic and Atmospheric Administration (NOAA)
843 for providing WOD data (<https://www.ncei.noaa.gov/products/world-ocean-database>), and the
844 European Centre for Medium-Range Weather Forecasts (ECMWF) for providing the ORAS5 data
845 (<https://cds.climate.copernicus.eu/datasets/reanalysis-oras5>).
846

847 **Author Contributions**

848 M.H. and Y.Z. conceived and designed the study. M.H. performed the research and wrote the initial
849 draft of this paper. M.H., X.X., and Y.Z. reviewed and edited the paper.
850

851 **Competing interests**

852 The authors declare that they have no competing interests.

853

854
855
856
857
858
859
860
861
862
863
864
865
866
867
868
869
870
871
872
873
874
875
876

877 **References**

- 878 Acharya S S, Panigrahi M K. Eastward shift and maintenance of Arabian Sea oxygen minimum zone:
879 Understanding the paradox. *Deep Sea Research Part I: Oceanographic Research Papers*, **2016**,
880 115: 240-252.
- 881 Akiba T, Sano S, Yanase T, et al. Optuna: A next-generation hyperparameter optimization framework.
882 *Proceedings of the 25th ACM SIGKDD international conference on knowledge discovery & data*
883 *mining*, **2019**: 2623-2631.
- 884 Bergmeir C, Benítez J M. On the use of cross-validation for time series predictor evaluation.
885 *Information Sciences*, **2012**, 191: 192-213.
- 886 Berman-Frank I, Chen Y B, Gao Y, et al. Feedbacks between the nitrogen, carbon and oxygen cycles.
887 *Nitrogen in the marine environment. Amsterdam The Netherlands: Elsevier Inc*, **2008**, 1537-
888 63.
- 889 Bittig H C, Körtzinger A. Update on response times, in-air measurements, and in situ drift for oxygen
890 optodes on profiling platforms. *Ocean Science*, **2017**, 13(1): 1-11.
- 891 Bittig H C, Körtzinger A, Neill C, et al. Oxygen optode sensors: principle, characterization, calibration,
892 and application in the ocean. *Frontiers in Marine Science*, **2018**, 4: 429.
- 893 Bopp L, Resplandy L, Orr J C, et al. Multiple stressors of ocean ecosystems in the 21st century:
894 projections with CMIP5 models. *Biogeosciences*, **2013**, 10(10): 6225-6245.
- 895 Breiman L. Random forests. *Machine learning*, **2001**, 45: 5-32.

896 Breitburg D, Levin L A, Oschlies A, et al. Declining oxygen in the global ocean and coastal waters.
897 *Science*, **2018**, 359(6371): eaam7240.

898 [Brunsdon C, Fotheringham A S, Charlton M E. Geographically weighted regression: a method for
899 exploring spatial nonstationarity. *Geographical analysis*, **1996**, 28\(4\): 281-298.](#)

900 [Busecke J J M, Resplandy L, Dunne J P. The equatorial undercurrent and the oxygen minimum zone
901 in the Pacific. *Geophysical Research Letters*, **2019**, 46\(12\): 6716-6725.](#)

902 Carstensen J, Andersen J H, Gustafsson B G, et al. Deoxygenation of the Baltic Sea during the last
903 century. *Proceedings of the National Academy of Sciences*, **2014**, 111(15): 5628-5633.

904 Chen T, Guestrin C. Xgboost: A scalable tree boosting system. *Proceedings of the 22nd acm sigkdd
905 international conference on knowledge discovery and data mining*. **2016**: 785-794.

906 Cocco V, Joos F, Steinacher M, et al. Oxygen and indicators of stress for marine life in multi-model
907 global warming projections. *Biogeosciences*, **2013**, 10(3): 1849-1868.

908 Deutsch C, Brix H, Ito T, et al. Climate-forced variability of ocean hypoxia. *Science*, **2011**, 333(6040):
909 336-339.

910 Dietterich T G. Ensemble methods in machine learning. *International workshop on multiple
911 classifier systems. Berlin, Heidelberg: Springer Berlin Heidelberg*, **2000**: 1-15.

912 [Duteil O, Frenger I, Getzlaff J. The riddle of eastern tropical Pacific Ocean oxygen levels: the role of
913 the supply by intermediate-depth waters. *Ocean Science*, **2021**, 17\(5\): 1489-1507.](#)

914 [Espinoza-Morriberón D, Echevin V, Colas F, et al. Oxygen variability during ENSO in the tropical
915 South Eastern Pacific. *Frontiers in Marine Science*, **2019**, 5: 526.](#)

916 Frajka-Williams E, Rhines P B, Eriksen C C. Physical controls and mesoscale variability in the
917 Labrador Sea spring phytoplankton bloom observed by Seaglider. *Deep Sea Research Part I:
918 Oceanographic Research Papers*, **2009**, 56(12): 2144-2161.

919 Friedman J H. Greedy function approximation: a gradient boosting machine. *Annals of statistics*,
920 **2001**: 1189-1232.

921 Gade K. A non-singular horizontal position representation. *The journal of navigation*, **2010**, 63(3):
922 395-417.

923 Garcia, Hernan E., et al. *World Ocean Atlas 2023, Volume 3: Dissolved Oxygen, Apparent Oxygen
924 Utilization, Dissolved Oxygen Saturation and 30-year Climate Normal*. **2024**.

925 Geurts P, Ernst D, Wehenkel L. Extremely randomized trees. *Machine learning*, **2006**, 63: 3-42.

926 Giglio D, Lyubchich V, Mazloff M R. Estimating oxygen in the Southern Ocean using Argo
927 temperature and salinity. *Journal of Geophysical Research: Oceans*, **2018**, 123(6): 4280-4297.

928 Gouretski V, Cheng L, Du J, et al. A consistent ocean oxygen profile dataset with new quality control
929 and bias assessment. *Earth System Science Data*, **2024**, 16(12): 5503-5530.

930 Gruber N. The dynamics of the marine nitrogen cycle and its influence on atmospheric CO 2
931 variations. *The ocean carbon cycle and climate*. Springer Netherlands, **2004**, 97-148.

932 Gruber N. Warming up, turning sour, losing breath: ocean biogeochemistry under global change.
933 *Philosophical Transactions of the Royal Society A: Mathematical, Physical and Engineering
934 Sciences*, **2011**, 369(1943): 1980-1996.

935 Guryanov A. Histogram-based algorithm for building gradient boosting ensembles of piecewise
936 linear decision trees. *Analysis of Images, Social Networks and Texts: 8th International
937 Conference, AIST 2019, Kazan, Russia, July 17–19, 2019, Revised Selected Papers 8*. Springer
938 International Publishing, **2019**: 39-50.

939 Han M, Zhou Y. Global Monthly Dissolved Oxygen Reconstruction via Bayesian Ensemble Machine

940 Learning. Zenodo, **2026**. <https://doi.org/10.5281/zenodo.19705526>~~2025-~~
941 <https://doi.org/10.5281/zenodo.17548659>

942 Helm K P, Bindoff N L, Church J A. Observed decreases in oxygen content of the global ocean.
943 *Geophysical Research Letters*, **2011**, 38(23).

944 Huang S, Shao J, Chen Y, et al. Reconstruction of dissolved oxygen in the Indian Ocean from 1980
945 to 2019 based on machine learning techniques. *Frontiers in Marine Science*, **2023**, 10:
946 1291232.

947 [Iida T, Odate T, Fukuchi M. Long-term trends of nutrients and apparent oxygen utilization south of](#)
948 [the polar front in Southern Ocean intermediate water from 1965 to 2008. *PLoS one*, **2013**, 8\(8\):](#)
949 [e71766.](#)

950 Ito T, Cervania A, Cross K, et al. Mapping dissolved oxygen concentrations by combining shipboard
951 and Argo observations using machine learning algorithms. *Journal of Geophysical Research:*
952 *Machine Learning and Computation*, **2024**, 1(3): e2024JH000272.

953 Jain V, Shankar D, Vinayachandran P N, et al. Evidence for the existence of Persian Gulf water and
954 Red Sea water in the Bay of Bengal. *Climate dynamics*, **2017**, 48(9): 3207-3226.

955 Karstensen J, Stramma L, Visbeck M. Oxygen minimum zones in the eastern tropical Atlantic and
956 Pacific oceans. *Progress in Oceanography*, **2008**, 77(4): 331-350.

957 Ke G, Meng Q, Finley T, et al. Lightgbm: A highly efficient gradient boosting decision tree. *Advances*
958 *in neural information processing systems*, **2017**, 30.

959 Keeling R F, Körtzinger A, Gruber N. Ocean deoxygenation in a warming world. *Annual review of*
960 *marine science*, **2010**, 2: 199-229.

961 [Kleiber W, Raftery A E, Baars J, et al. Locally calibrated probabilistic temperature forecasting using](#)
962 [geostatistical model averaging and local Bayesian model averaging. *Monthly Weather Review*,](#)
963 [2011, 139\(8\): 2630-2649.](#)

964 Kolber Z S, Van Dover C L, Niederman R A, et al. Bacterial photosynthesis in surface waters of the
965 open ocean. *Nature*, **2000**, 407(6801): 177-179.

966 Kwiatkowski L, Torres O, Bopp L, et al. Twenty-first century ocean warming, acidification,
967 deoxygenation, and upper-ocean nutrient and primary production decline from CMIP6 model
968 projections. *Biogeosciences*, **2020**, 17(13): 3439-3470.

969 Long M C, Deutsch C, Ito T. Finding forced trends in oceanic oxygen. *Global Biogeochemical Cycles*,
970 **2016**, 30(2): 381-397.

971 Mao Z, Mao Z, Jamet C, et al. Seasonal cycles of phytoplankton expressed by sine equations using
972 the daily climatology from satellite-retrieved chlorophyll-a concentration (1997–2019) over
973 global ocean. *Remote Sensing*, **2020**, 12(16): 2662.

974 Matear R J, Hirst A C. Long-term changes in dissolved oxygen concentrations in the ocean caused
975 by protracted global warming. *Global Biogeochemical Cycles*, **2003**, 17(4).

976 Mishonov A.V., T. P. Boyer, O. K. Baranova, et al. World Ocean Database 2023. C. Bouchard, Technical
977 Ed., *NOAA Atlas NESDIS 97*, 206 pp, **2024**.

978 [Morrison A K, Waugh D W, Hogg A M C, et al. Ventilation of the Southern Ocean pycnocline. *Annual*](#)
979 [Review of Marine Science](#), **2022**, 14: 405-430.

980 Naqvi S W A, Naik H, Pratihary A, et al. Coastal versus open-ocean denitrification in the Arabian
981 Sea. *Biogeosciences*, **2006**, 3(4): 621-633.

982 [Narvekar J, Kesserkar P, Sreejith K S, et al. Recent oxygenation of oxygen minimum zone in the](#)
983 [Arabian Sea and possible causes. *Progress in Oceanography*, **2025**: 103600.](#)

984 [Nayak A A, Vinayachandran P N, George J V. Arabian Sea high salinity core supplies oxygen to the](#)
985 [Bay of Bengal. *Deep Sea Research Part II: Topical Studies in Oceanography*, **2025**, 221: 105477.](#)
986 Olsen A, Key R M, Van Heuven S, et al. The Global Ocean Data Analysis Project version 2
987 (GLODAPv2)—an internally consistent data product for the world ocean. *Earth System Science*
988 *Data*, **2016**, 8(2): 297-323.
989 Oschlies A, Brandt P, Stramma L, et al. Drivers and mechanisms of ocean deoxygenation. *Nature*
990 *Geoscience*, **2018**, 11(7): 467-473.
991 Pathak R, Dasari H P, Ashok K, et al. Effects of multi-observations uncertainty and models similarity
992 on climate change projections. *npj Climate and Atmospheric Science*, **2023**, 6(1): 144.
993 Paulmier A, Ruiz-Pino D. Oxygen minimum zones (OMZs) in the modern ocean. *Progress in*
994 *oceanography*, **2009**, 80(3-4): 113-128.
995 Prokhorenkova L, Gusev G, Vorobev A, et al. CatBoost: unbiased boosting with categorical features.
996 *Advances in neural information processing systems*, **2018**, 31.
997 [Raftery A E, Gneiting T, Balabdaoui F, et al. Using Bayesian model averaging to calibrate forecast](#)
998 [ensembles. *Monthly weather review*, **2005**, 133\(5\): 1155-1174.](#)
999 Reichstein M, Camps-Valls G, Stevens B, et al. Deep learning and process understanding for data-
1000 driven Earth system science. *Nature*, **2019**, 566(7743): 195-204.
1001 Rippeth T, Shen S, Lincoln B, et al. The deepwater oxygen deficit in stratified shallow seas is
1002 mediated by diapycnal mixing. *Nature communications*, **2024**, 15(1): 3136.
1003 Roach, C. J., Bindoff, N. L. Developing a new oxygen atlas of the world's oceans using data
1004 interpolating variational analysis. *Journal of Atmospheric and Oceanic Technology*,
1005 **2023**, 40(11): 1475-1491.
1006 Roberts D R, Bahn V, Ciuti S, et al. Cross-validation strategies for data with temporal, spatial,
1007 hierarchical, or phylogenetic structure. *Ecography*, **2017**, 40(8): 913-929.
1008 Roch M, Brandt P, Schmidtko S. Recent large-scale mixed layer and vertical stratification maxima
1009 changes. *Frontiers in Marine Science*, **2023**, 10: 1277316.
1010 Ryther J H. Photosynthesis in the Ocean as a Function of Light Intensity 1. *Limnology and*
1011 *Oceanography*, **1956**, 1(1): 61-70.
1012 Sampaio E, Santos C, Rosa I C, et al. Impacts of hypoxic events surpass those of future ocean
1013 warming and acidification. *Nature Ecology & Evolution*, **2021**, 5(3): 311-321.
1014 Sarma V, Udaya Bhaskar T V S. Ventilation of oxygen to oxygen minimum zone due to anticyclonic
1015 eddies in the Bay of Bengal. *Journal of Geophysical Research: Biogeosciences*, **2018**, 123(7):
1016 2145-2153.
1017 Schmidt H, Czeschel R, Visbeck M. Ventilation dynamics of the oxygen minimum zone in the Arabian
1018 Sea. *Biogeosciences Discussions*, **2019**, 2019: 1-32.
1019 Schmidtko, S., Stramma, L. & Visbeck, M. Decline in global oceanic oxygen content during the past
1020 five decades. *Nature*, **2017**, 542(7641): 335-339.
1021 Shao J, Huang S, Chen Y, et al. Satellite-based global sea surface oxygen mapping and interpretation
1022 with spatiotemporal machine learning. *Environmental Science & Technology*, **2023**, 58(1): 498-
1023 509.
1024 Sharp J D, Fassbender A J, Carter B R, et al. GOBAI-O2: temporally and spatially resolved fields of
1025 ocean interior dissolved oxygen over nearly 2 decades. *Earth System Science Data*, **2023**, 15,
1026 4481–4518, <https://doi.org/10.5194/essd-15-4481-2023>.
1027 Shen C. A transdisciplinary review of deep learning research and its relevance for water resources

1028 scientists. *Water Resources Research*, **2018**, 54(11): 8558-8593.

1029 [Shenoy D M, Suresh I, Uskaikar H, et al. Variability of dissolved oxygen in the Arabian Sea Oxygen](#)
1030 [Minimum Zone and its driving mechanisms. *Journal of Marine Systems*, **2020**, 204: 103310.](#)

1031 Solomon A, Heuzé C, Rabe B, et al. Freshwater in the arctic ocean 2010–2019. *Ocean Science*, **2021**,
1032 17(4): 1081-1102.

1033 Stramma L, Johnson G C, Sprintall J, et al. Expanding oxygen-minimum zones in the tropical oceans.
1034 *Science*, **2008**, 320(5876): 655-658.

1035 Stramma L, Prince E D, Schmidtko S, et al. Expansion of oxygen minimum zones may reduce
1036 available habitat for tropical pelagic fishes. *Nature Climate Change*, **2012**, 2(1): 33-37.

1037 Stramma L, Schmidtko S, Levin L A, et al. Ocean oxygen minima expansions and their biological
1038 impacts. *Deep Sea Research Part I: Oceanographic Research Papers*, **2010**, 57(4): 587-595.

1039 Talley L D. Closure of the global overturning circulation through the Indian, Pacific, and Southern
1040 Oceans: Schematics and transports. *Oceanography*, **2013**, 26(1): 80-97.

1041 Tang W, Li Z, Cassar N. Machine learning estimates of global marine nitrogen fixation. *Journal of*
1042 *Geophysical Research: Biogeosciences*, **2019**, 124(3): 717-730.

1043 Wang Z, Garcia H E, Boyer T P, et al. Bias Evaluation for Sensor-Based Dissolved Oxygen from CTD
1044 and Profiling Floats in the World Ocean Database. *Journal of Atmospheric and Oceanic*
1045 *Technology*, **2025**, 42(10): 1263-1280.

1046 Wong A P S, Wijffels S E, Riser S C, et al. Argo data 1999–2019: Two million temperature-salinity
1047 profiles and subsurface velocity observations from a global array of profiling floats. *Frontiers*
1048 *in Marine Science*, **2020**, 7: 700.

1049 Wu Y, Zheng Z, Chen X, et al. Amplified warming accelerates deoxygenation in the Arctic Ocean.
1050 *Nature Climate Change*, **2025**, 15(8): 859-865.

1051 Zhang Z, Ma W, Chai F. Role of ocean circulation and settling of particulate organic matter in the
1052 decoupling between the oxygen minimum zone and the phytoplankton productive zone in the
1053 Arabian Sea: A modeling study. *Frontiers in Marine Science*, **2022**, 9: 927921.

1054 Zhou Y, Gong H, Zhou F. Responses of horizontally expanding oceanic oxygen minimum zones to
1055 climate change based on observations. *Geophysical Research Letters*, **2022**, 49(6):
1056 e2022GL097724.

1057

1058

1059